1 **Title**
2 Conserved principles of spatial biology define tumor heterogeneity and response to
3 immunotherapy
4
5 **Authors**
6 Vivek Behera[1,2], Hannah Giba[2,3], Ue-Yu Pen[2,3], Anna Di Lello[1], Benjamin A. Doran[2,4],
7 Alessandra Esposito[1], Apameh Pezeshk[1], Christine M. Bestvina[1], Justin Kline[1], Marina C.
8 Garassino[1], Arjun S. Raman[2,3,5]
9
10 **Affiliations**
11 [1]Department of Medicine, Section of Hematology/Oncology, University of Chicago, Chicago, IL,
12 60637
13 [2]Duchossois Family Institute, University of Chicago, Chicago, IL, 60637
14 [3]Department of Pathology, University of Chicago, Chicago, IL, 60637
15 [4]Pritzker School of Molecular Engineering, University of Chicago, Chicago, IL, 60637
16 [5]Center for the Physics of Evolving Systems, University of Chicago, Chicago, IL, 60637

Abstract

The tumor microenvironment (TME) is an immensely complex ecosystem[1,2]. This complexity underlies difficulties in elucidating principles of spatial organization and using molecular profiling of the TME for clinical use[3]. Through statistical analysis of 96 spatial transcriptomic (ST-seq) datasets spanning twelve diverse tumor types, we found a conserved distribution of multicellular, transcriptionally covarying units termed 'Spatial Groups' (SGs). SGs were either dependent on a hierarchical local spatial context – enriched for cell-extrinsic processes such as immune regulation and signal transduction – or independent from local spatial context – enriched for cell-intrinsic processes such as protein and RNA metabolism, DNA repair, and cell cycle regulation. We used SGs to define a measure of gene spatial heterogeneity – 'spatial lability' – and categorized all 96 tumors by their TME spatial lability profiles. The resulting classification captured spatial variation in cell-extrinsic versus cell-intrinsic biology and motivated class-specific strategies for therapeutic intervention. Using this classification to characterize pre-treatment biopsy samples of 16 non-small cell lung cancer (NSCLC) patients outside our database distinguished responders and non-responders to immune checkpoint blockade while programmed death-ligand 1 (PD-L1) status and spatially unaware bulk transcriptional markers did not. Our findings show conserved principles of TME spatial biology that are both biologically and clinically significant.

Main

The tumor microenvironment (TME) is a complex milieu of interacting cells, proteins, and other biological components that influences critical properties of tumor biology such as growth, metastasis, and response to therapy[1,2]. Biological variation within the TME reflects clinically relevant differences across genetic, pathway, cellular, and tissue-level scales[4,5]. For instance, recent studies have shown the prognostic and predictive power of TME-specific biomarkers such as tumor infiltrating lymphocyte (TIL) score in melanoma and 'Immunoscore' – the spatial balance of CD3+ and CD8+ T cell density – in colorectal cancer[6–10]. These and other similar findings have motivated significant investment in studying the TME as an ecosystem of cells interacting within the spatial constraints of a tumor, most notably with technologies that couple cellular information about RNA or protein levels with cellular spatial locations[11]. Such spatial molecular profiling studies conducted in a variety of tumor types have revealed a common theme: the substantial heterogeneity within tumors (intratumoral) and across tumors (intertumoral) makes elucidating organizing principles of the TME very challenging[3]. By extension, the clinical utility of TME spatial profiling has been limited in scope.

Recent efforts have begun to outline a strategy to learn conserved aspects of TME spatial biology with the idea that these aspects reflect organizing principles of biological interest. These studies have collectively demonstrated the existence of recurrent multicellular spatial structures associated with tumor biology – somatic mutations, cell cycle synchrony, invasive fronts – and with cancer prognosis[12–17]. Obtaining these insights relied on imaging-based technologies that query tens of proteins to identify phenotypes such as cell type, cell cycle state, and a limited set of cell functional states. While these studies have been invaluable in demonstrating the relevance of spatial organization for TME biology, it has remained unclear whether a broader and more unbiased assessment of cellular phenotypes might demonstrate general principles of TME spatial organization. Spatial transcriptomics ('ST-seq') and related technologies, which provide genome-wide transcriptional information coupled to nearly single-

61   cell-resolution of spatial coordinates, enable broad and unbiased assessment of TME spatial

62   biology. However, the complexity of such data has precluded moving beyond mere description

63   into an elucidation of spatial biology principles[18].

64   Advances in statistical inference developed in other fields of biology – protein science,

65   genomics, and microbiome science – provide useful frameworks for addressing this challenge.

66   For instance, at the scale of proteins, analysis of conserved amino acid covariation within

67   ensembles of related proteins has yielded protein 'sectors' – groups of amino acids that are

68   critical for engineering synthetically folded and functional proteins[19–22]. At the scale of genomes,

69   covariation analysis of gene content across extant diversity within kingdoms of life has revealed

70   units of collective protein-protein interactions that are critical for behavior and organismal

71   fitness[23–26]. At the scale of microbiomes, covariation between bacterial taxa across individuals

72   has yielded 'ecogroups' – groups of taxa that are of functional and clinical significance amongst

73   humans[27–29]. Thus, these studies have established a general strategy for parsing organization

74   amongst complex biological systems: first identify an ensemble of systems, then statistically

75   deduce features that are conserved across the ensemble.

76   Using such studies as inspiration, we hypothesized that statistical analysis of ST-seq

77   data across a diverse ensemble of solid tumors – a 'pan-tumor' database – would reveal

78   conserved patterns of TME spatial biology in an unbiased manner. Our results showed that all

79   TMEs shared the presence of multicellular groups of transcriptionally covarying spots, 'Spatial

80   Groups' (SGs), with expression profiles that are either dependent (defined as 'nested Spatial

81   Groups', NSGs) or independent (defined as 'non-nested Spatial Groups', non-NSGs) on their

82   local spatial environments. We found that NSG biology obeys a characteristic pattern: variation

83   in local-scale biological processes, such as cell adhesion, are nested within the spatial context

84   of larger-scale processes, such as T cell infiltration. We compressed SGs into a tumor-wide

85   measure of spatial heterogeneity in gene expression that we termed 'spatial lability'. This

86   enabled the comparison of spatial biology across our ensemble of tumors. The resulting

87   classification distinguished biologically and clinically relevant elements of immune regulation,

88   cell signaling, DNA repair, protein and RNA metabolism, and cell cycle regulation. To

89   interrogate the clinical applicability of our findings, we performed ST-seq on 16 'out-of-sample'

90   pre-treatment biopsy samples of patients with metastatic non-small cell lung cancer (NSCLC)

91   who received immune checkpoint blockade (ICB) therapy and were not within our pan-tumor

92   database. Using the pan-tumor spatial lability classification to describe these samples, we found

93   that immune spatial lability distinguished patient response to ICB therapy while standard and

94   previously described spatially unaware markers – PD-L1 status, bulk transcriptional differences,

95   and existing gene sets – did not.

96   Overall, our findings revealed conserved principles of TME spatial biology that are

97   biologically and clinically meaningful. Our results motivate further interrogation into the nature of

98   collective spatial organization within the TME and open the possibility for interpretable statistical

99   models of clinical endpoints using spatial biology.

100

101   _Spatial Groups (SGs) define a conserved architecture of TME spatial biology_

102   As our goal was to discover organizing principles of TME spatial biology, we sought to

103   construct a mapping that could infer TME spatial organization from ST-seq transcriptional data.

104   Each dataset we studied was created using 10X Visium technology, which generates

105   transcriptome-wide measurements for up to 14,000 spatial locations (called spots, each of

106   which contains multiple cells) in up to an 11 mm x 11 mm region of biopsy tissue[30]. Previous

107   literature has demonstrated the presence and importance of spatially nested and non-nested

108   biological processes in the TME[17,31]. As such, we wanted our mapping to simultaneously

109   capture and distinguish nested and non-nested biological processes – a quality that currently

110   developed frameworks for ST-seq data do not contain (**Fig. 1A**)[32–37]. We therefore developed a

111   new framework called 'TumorSPACE' (Tumor Spatial Architectures from the Complete

112   Eigenspectrum). While this framework is described in detail in Methods, TumorSPACE first uses

113   patterns of transcriptional covariation to define hierarchical relationships between ST-seq

114   spots[26,38]. This yields a tree-like relationship between all spots in the TME where each leaf of

115   the tree defines an individual spot and branchpoints in the tree group spots together that are

116   transcriptionally similar. TumorSPACE then removes branches of that tree that do not relate to

117   spatial organization (**Extended Data Fig. 1A**). This resulting tree is a dataset-specific

118   'TumorSPACE map' between transcriptional information and spatial organization.

119   We applied TumorSPACE to a diverse database of 96 tumors profiled by ST-seq and

120   used the resulting maps to infer the spatial locations of spots (Methods). Each dataset in our

121   database represented a unique patient sample; the database spanned 12 distinct tumor types,

122   multiple disease stages (localized versus metastatic), and multiple tumor body locations

123   (primary, metastatic lymph node, metastatic organ) (**Extended Data Fig. 1B**, **Supplementary**

124   **Table 1**). We found that for all datasets, the TumorSPACE maps significantly inferred spot

125   spatial locations ($q < 0.01$) (**Fig. 1B**, Methods). Thus, TumorSPACE maps accurately related

126   transcriptional and spatial information within TMEs.

127   We next interrogated whether the TumorSPACE maps revealed any underlying

128   conserved principles of TME spatial organization. We first focused on the best-performing

129   TumorSPACE map, a small-cell ovarian cancer dataset 'SCOC-P2'. Branchpoints in this map

130   defined groups of spots that were anisotropically distributed in the biopsy sample and comprised

131   spots that were either (i) physically separated from each other or (ii) were spatially nested within

132   other groups of spots defined by the TumorSPACE map. We therefore termed the branchpoints

133   of TumorSPACE maps 'Spatial Groups' (SGs). We defined any SG that was spatially nested

134   within its parent SG – the SG one layer closer to the root of the map – as a nested Spatial

135   Group (NSG). Any SG that was not spatially nested within its parent was a non-nested Spatial

136   Group (non-NSG) (**Fig. 1C**). We found that in the SCOC-P2 dataset, NSGs could be spatially

137   nested to varying degrees. We therefore defined 'NSG depth' for any NSG as the following: as

138   one moves from an NSG towards the root of the TumorSPACE map, 'NSG depth' is the number

139   of NSGs that are encountered inclusive of the original NSG prior to arriving at a non-NSG

140   (**Extended Data Fig. 1C**) (Methods). A systematic analysis of all tumors in our database

141   revealed a spatial architecture of the TME that is broadly conserved: SGs are comprised of a

142   consistent distribution of non-NSGs and NSGs that can be nested up to several degrees (**Fig.**

143   **1D**).

144   We next sought to characterize the biology reflected by NSGs and non-NSGs. We

145   described TME biology using cell type distribution and cellular gene pathway usage since these

146   qualities have been implicated in TME spatial biology across many cancer types. At each SG,

147   we detected differential abundance of genes, pathways, and cell types (**Extended Data Fig.**

148   **2A**) (Methods). Since each spot consists of multiple cells, we used SpaCET for deconvoluting

149   cell types (Methods)[39]. We found a relationship between the spatial scale of SGs and biological

150   processes: SGs that were larger in spatial distribution displayed changes in cell type abundance

151   (particularly in CD4+ and CD8+ T cells) while SGs that were smaller in spatial distribution

152   displayed changes in pathway usage (particularly in pathways for cell adhesion, cell cycle, and

153   adaptive cytotoxicity) (**Extended Data Fig. 2B**).

154   As NSGs are nested within the local spatial context of their parent SGs, we asked how

155   much a differential process (pathway or cell type) within an NSG was dependent on biological

156   processes defined by the spatial context of its parent. For this, we quantified contextual

157   dependence as the odds ratio of detecting a change in a biological process within an NSG

158   ('Process B') given a particular change in a biological process ('Process A') at its parent SG. We

159   then computed whether any odds ratio was significantly different than 1. This measured whether

160   the associated set of parent-child processes was contextually dependent or independent (**Fig.**

161   **1E**, left) (Methods). We found that 74% of differential processes within an NSG were dependent

162   on the local spatial context defined by the parent SG, illustrating extensive biological nesting

163   within NSGs. Moreover, we found that certain biological processes were associated with

164   stronger local spatial contexts: NSG processes were nearly universally dependent on oncogenic

165   pathways in parent SGs yet were less frequently dependent on parent SG pathways that largely

166   involved direct cell-cell contacts, such as cell adhesion and immune cytotoxicity (**Fig. 1E**, right;

167   **Extended Data Fig. 2C**). Additionally, the strength of local spatial context associated with a

168   biological process within a parent SG – an averaged odds ratio across all processes – was

169   linearly related to the spatial scale of the parent NSG (**Fig. 1F**, top). Thus, as parent SGs

170   became larger, their influence on biological processes encoded within NSGs became greater. In

171   contrast, no such relationship was present when considering the influence of biological

172   processes in non-NSGs on their local spatial environment (**Fig. 1F**, bottom). These results

173   demonstrated that NSGs reflect nested biological properties.

174   Overall, our findings revealed a general spatial architecture of TMEs. TMEs are

175   hierarchically organized into multicellular units of transcriptional covariation, 'Spatial Groups',

176   that can be either spatially nested (NSGs) or non-nested (non-NSGs). The spatial organization

177   of NSGs reflects the contextual dependence of smaller-scale biological processes involving cell-

178   cell interactions, amongst larger-scale biological processes such as cell type abundance (**Fig.**

179   **1G**). These findings motivated using SGs as a common unit of spatial organization for

180   investigating heterogeneity in TME spatial biology.

181

182   _Using SGs to define spatial lability in TMEs_

183   To capture variation in gene expression patterns amongst SGs in a holistic manner, we

184   defined gene 'spatial lability' – the extent of change of gene expression when comparing across

185   partitions of the TME. We first identified all SGs for a given TME. Then, for a given gene, we

186   isolated the SGs and associated ST-seq spots where the gene was differentially expressed

187   (**Fig. 2A**, top). Finally, we computed the fraction of the tumor dataset represented by those ST-

188   seq spots and termed this fraction the 'spatial lability' (SLAB) score for the gene of interest (**Fig.**

189   **2A**, bottom) (Methods). A comparison of SLAB scores with gene expression for all genes across

190   all tumors in our database illustrated that SLAB scores were positively correlated with average

191   gene expression but also captured other modes of gene-level spatial variation. For example,

192   genes with low average expression exhibited variation in SLAB score (**Fig. 2B**). Furthermore,

193   77% of genes had no correlation between bulk gene expression and SLAB score when

194   comparing across tumors (**Extended Data Fig. 3**). As a specific example, the calreticulin gene

195   (CALR) had similar bulk expression levels in 3 selected tumors, yet its SLAB score varied from

196   high to low across these tumors (**Fig. 2C**). Visualization of CALR expression across the TME

197   clearly illustrated that the degree of spatial heterogeneity in gene expression followed the

198   degree of spatial lability across tumors (**Fig. 2D**). Examination of the SGs associated with

199   differential expression of CALR showed that the high spatial lability tumor contained changes in

200   CALR expression at both large- and medium-sized SGs, while the tumors with lower SLAB

201   scores had SG changes restricted to medium and small SGs (**Fig. 2E**). Together, these data

202   demonstrate that the SLAB score captures information about the spatial heterogeneity of gene

203   expression across the TME that is distinct from bulk gene expression.

204   To validate that SLAB scores captured spatial heterogeneity in the TME, we compared

205   SLAB scores with an orthogonal measure of spatial biology – multiplexed immunofluorescence

206   (mIF) across 51 marker genes – for two diffuse large B cell lymphoma (DLBCL) samples within

207   our pan-tumor database (Methods). We used a grid approach to define spatial domains of

208   varying sizes. Variation in cell type abundance was computed using the coefficient of variation

209   across these grids (**Extended Data Fig. 4A**) (Methods). This approach demonstrated cell types

210   to be more spatially labile in the DLBCL-P2 tumor (Patient 2) than in DLBCL-P1 (Patient 1)

211   (**Extended Data Fig. 4B**). SLAB scores, computed across SpaCET-deconvoluted cell type

212   proportions, recapitulated this finding (**Extended Data Fig. 4C**). Examination of IF intensity

213   distributions for CD3 (a pan T cell marker) and CD21 (an abundant B cell marker) demonstrated

214   that germinal center (GC) effacement might explain the inter-tumoral differences in cell type

215   spatial lability between the two DLBCL samples (**Extended Data Fig. 4D**). Moreover, we found

216   that SGs with simultaneous enrichment of T cells and depletion of B cells included many H&E-

217   identified GCs in DLBCL-P2 (**Extended Data Fig. 4E**).

218   Together, these results demonstrate that the SG-based metric we created – SLAB scores

219   – accurately captured information about the spatial heterogeneity of gene expression across

220   TMEs, thereby enabling spatially based comparisons between tumors.

221
222   *Classification of TMEs by spatial lability*

223   To compare TMEs by their profiles of spatial lability, we aligned the genome-wide SLAB

224   scores across for all tumors in our database and computed the Euclidean distance between

225   each pair of tumors (**Extended Data Fig. 5**). Hierarchical clustering of pairwise distance

226   between tumors defined a tree representing a pan-tumor classification where tumors were

227   grouped by similarity of their spatial lability profiles and branchpoints reflected signatures of

228   differential spatial lability between groups (**Fig. 3A,B**). Interrogation of the tree illustrated two

229   results. First, tumors were approximately ordered by their average spatial lability. In the

230   representation depicted in **Fig. 3B**, tumors ordered from left to right – labeled as groups A

231   through M – reflected a continuum of average SLAB scores from high to low respectively

232   (**Extended Data Fig. 6A**). As an example, while the average gene expression across all genes

233   for the group of tumors on the far right (group M) was higher than the other groups, the spatial

234   lability of genes in group M tumors was significantly lower than the other groups (**Extended**

235   **Data Fig. 6B**). Second, the resulting clusters illustrated that tumor groups were either uniform

236   (e.g. groups C and F) or varied (e.g. groups E, L, M) in their tissue of origin. For example, we

237   found that tumors originating in breast tissue (91% triple-negative, rest unknown) classified into

238   groups B, D, E, H, I, L, and M. Furthermore, we saw that group E were composed of tumors

239   originating in breast, skin, ovarian, and central nervous system (CNS) tissues. These results

240   suggested that patterns of spatial lability across our pan-tumor database described both tumor-

241   type-specific and tumor-type-agnostic differences in the TME.

242   We wanted to test whether the pan-tumor classification based on spatial lability captured

243   similarity in spatial organization at the level of individual spots. For this, we tested whether the

244   TumorSPACE map of one tumor (tumor A) could be used to predict the pairwise distances

245   between spots of another tumor (tumor B). We then compared whether the accuracy of such

246   predictions related to tumors being within the same or different spatial lability class. We

247   computed predictions by projecting the transcriptional data from tumor B into the TumorSPACE

248   map previously built for tumor A, which had not incorporated any information about tumor B. As

249   a result, pairwise spot-spot distances were predicted between all spots in tumor B. These

250   predictions were then compared to the actual pairwise distances between spots in tumor B

251   (**Extended Data Fig. 7A**) (Methods). We excluded group M tumors from this analysis since our

252   results showed that these tumors lacked spatial lability altogether. Overall, we found that 52% of

253   such tumor pairs predicted spot distance information better than null models. Additionally,

254   models were more likely to be predictive when selecting two tumors from the same spatial

255   lability class than from different classes (67% versus 49%), similar to the prediction increase

256   when comparing tumors of the same type versus different type (65% versus 47%) (**Extended

257   Data Fig. 7B**). In accord with this finding, spatial lability was an independent contributor to

258   cross-tumor spatial prediction from tumor type, suggesting that classes of tumors defined by

259   profiles of spatial lability reflect shared spatial organization even when composed of diverse

260   tumors (**Extended Data Fig. 7C**). Thus, while our pan-tumor database lacked the IHC

261   information required for comparison to clinical classification schemes such as TIL score and

262   Immunoscore, our analysis of the tree in **Fig. 3B** illustrated a classification of tumors by their

263   spatial biology that was not oriented merely by tumor type. This motivated further investigation

264   into the spatial lability changes that separated tumor groups.

265   We interrogated differences at branchpoints of the spatial lability classification (e.g. group

266   A versus group nA) using multiple complementary approaches – gene-level SLAB differences,

267   pathway-level SLAB differences using over-representation analysis (ORA), and pathway-level

268   SLAB differences using gene-set enrichment analysis (GSEA). The results we report for each of

269   these analyses were robust to gene co-linearity and multiple hypothesis testing (Methods). Four

270   branchpoints contained statistically significant differences in spatial lability amongst genes (**Fig.**

271   **3C**, left panel). We therefore performed an in-depth analysis at these four branchpoints of the

272   genes and pathways underlying differences in spatial lability (**Supplementary Table 2**).

273   Two of these branchpoints defined groups of tumors – C and E – that exhibited significant

274   changes in spatial lability associated with TME immune biology. Group C was comprised of a

275   set of exclusively primary CNS tumors and exhibited increased spatial lability of

276   neurotransmitter activity genes (GRIK1, KCNN2) and of complement activation pathways (**Fig.**

277   **3C**, top row). Notably, complement activation has been implicated in promoting glioma cell

278   proliferation and neovascularization in the hypoxic TME characteristically found in such tumors

279   as well as in mediating the suppression of anti-tumor immunity in both CNS tumors and non-

280   CNS tumor types[40]. Group E tumors, comprised of a diverse mixture of tumor types, showed

281   increased spatial lability of genes associated with immune exhaustion through diverse

282   mechanisms such as myeloid cell activation (P2RY11), TGF-β signaling (SMAD5), antigen

283   presentation (DPP9), innate immune cell activation (TRIM11, TRIM44), T cell migration (DPP9,

284   ELMO2), and T cell activation (STAT5, STAT5A, NFATC2IP, PLCG1, ORAI1) (**Fig. 3C**, second

285   row)[41–50]. Analysis of pathways demonstrated increased spatial lability in well-studied immune

286   signaling pathways (vesicle transport, solute carrier (SLC) transporters) as well as in pathways

287   linked to antigen generation (RNA metabolism, post-translational protein modifications),

288   suggesting that complementary biological processes collectively reflect immune spatial lability[51–

289   54]. Together, these data illustrated that group C and group E tumors have TMEs with increased

290   immune spatial lability via distinct components of TME immune biology.

291   The other two branchpoints defined groups of tumors – F and L – with spatial lability in

292   non-immune areas of TME biology as well as group M, the group notable for spatially invariant

293   biology across all studied genes and pathways. Group F was comprised of exclusively ovarian

294   tumors and had increased spatial lability for pathways related to olfactory receptors – a class of

295   cancer testis antigens that are abundantly expressed in ovarian tumors and are under

296   development as a CAR-T therapeutic target (**Fig. 3C**, third row)[55]. Group L, composed of

297   diverse tumors, demonstrated increased spatial lability for genes involved in mitochondrial

298   biology (MRPL40, LYRM1, MRPS14, NDUFS4, NFU1, MRPL21) as well as in RNA and protein

299   processing (COPS8, TCEAL8, RPAIN, ZCCHC17, SNW1, TTC1, KIAA1191, PEX19, GPN1,

300   PPIE) (**Fig. 3C**, fourth row panel). Accordingly, this group of tumors was enriched in spatial

301   lability for pathways related to cell-intrinsic processes – metabolism, transcriptional regulation,

302   and DNA repair.

303   We previously observed that cell-extrinsic versus cell-intrinsic processes were enriched in

304   NSGs and non-NSGs respectively (**Fig. 1F, G**). Having now observed that the spatial lability

305   classification varied across groups in enrichment for cell-extrinsic versus cell-intrinsic

306   processes, we hypothesized that the classification in **Fig. 3B** was reliant on information with

307   NSGs and non-NSGs to different degrees depending on tumor group. To test this idea, we

308   performed GSEA pathway enrichment at branchpoints E/nE and L/M using spots found within

309   only NSGs or within only non-NSGs. We examined these branchpoints because they

310   demonstrated enrichment for cell-extrinsic and cell-intrinsic biology respectively. We found that

311   NSGs alone identified 69% of pathways enriched by GSEA for spatial lability in Group E, while

312   non-NSGs alone did not identify any of these pathways. Conversely, non-NSGs alone identified

313   42% of pathways enriched for spatial lability in Group L, while NSGs alone did not identify any

314   of these pathways (**Fig. 3D**). Notably, 31% and 58% of pathways with altered spatial lability in

315   groups E and L, respectively, required transcriptional information contained within both NSGs

316   and non-NSGs. Furthermore, across all studied branchpoints we found that the likelihood of a

317   pathway exhibiting detectable changes in spatial lability within NSGs versus non-NSGs

318   depended on whether the pathway described cell-extrinsic or cell-intrinsic processes (**Fig. 3E**).

319   Together, these results illustrated a pan-tumor classification defined by spatial lability. The

320   biological variation associated with this classification distinguished cell-extrinsic processes – i.e.

321   immune signaling – that are found mostly within NSGs versus cell-intrinsic processes like DNA

322   repair found in both NSGs and non-NSGs. Interrogation of genes and pathways distinguishing

323   groups also showed spatial lability in targets with proven therapeutic significance. Together,

324   these findings motivated using our pan-tumor classification schema to predict the clinical

325   outcome of patients whose tumors were not contained within our tumor database.

326

327   *Pan-tumor TME classification by spatial lability distinguishes response to immunotherapy in*

328   *metastatic NSCLC*

329   As two branchpoints in our pan-tumor classification demonstrated variation in immune

330   spatial lability, we hypothesized that classification of a separate cohort of tumors by immune

331   spatial lability could be used to predict patient response to anti-PD1/anti-PD-L1 immune

332   checkpoint blockade (ICB) – a widely approved therapeutic modality across diverse solid

333   tumors. To this end, we focused our efforts on patients diagnosed with metastatic NSCLC.

334   Despite substantial improvements in overall survival with the use of ICB therapies in the

335   metastatic NSCLC frontline setting, 5-year overall survival remains quite poor at 19%[56].

336   Moreover, the only clinically approved biomarker of response to ICB therapy, PD-L1

337   immunohistochemistry (IHC), is weakly predictive of outcomes in the frontline metastatic setting

338   for NSCLC, prompting ongoing studies on whether gene expression or cell type abundance

339   biomarkers might be more predictive of such outcomes[5,56–58].

340   To address whether spatial lability informs ICB response, we conducted a retrospective

341   pilot study of 16 patients with metastatic NSCLC without targetable mutations who received

342   frontline ICB with or without chemotherapy (Methods). For each patient, we conducted ST-seq

343   on pre-treatment biopsy samples followed by (i) computing genome-wide SLAB profiles for all

344   samples and (ii) contextualizing the resulting data using the pan-tumor classification of tumor

345   spatial lability defined by the discovery cohort in **Fig. 3B**. We also performed

346   immunohistochemistry (IHC) to determine PD-L1 tumor proportion score on the same pre-

347   treatment diagnostic biopsy sample. We then evaluated whether classification by spatial lability

348   or PD-L1 status could predict Progression-Free Survival (PFS) after ICB treatment (**Fig. 4A**).

349   Two possible variables were identified that could confound an association with ICB response:

350   ICB regimen choice and presence of the somatic mutation KRAS G12C, which is targetable in

351   the second line (**Extended Data Fig. 8A,B**). Univariate analysis found that neither variable was

352   associated with PFS, excluding the possibility that these factors influenced our study (**Extended**

353   **Data Fig. 8C**).

354   To evaluate this out-of-sample validation cohort of NSCLC tumors within the context of our

355   pan-tumor classification from **Fig. 3B**, we first used TumorSPACE to identify SGs for each

356   NSCLC tumor. We found a similar distribution of nested and non-nested SGs as within our pan-

357   tumor database, illustrating the generalizability of the distribution of SGs in TMEs (**Extended**

358   **Data Fig. 9**). Comparison of spatial lability profiles between the NSCLC tumors and the pan-

359   tumor database defined two groups. One group, comprised of twelve NSCLC tumors, exhibited

360   a spatial lability profile similar to group C and group E tumors in our pan-tumor classification –

361   high spatial lability amongst immune-related components ('immune spatially labile', 'ISL'). The

362   other group, comprised of four NSCLC tumors, exhibited a spatial lability profile similar to group

363   L and group M tumors – low spatial lability in immune biology ('immune spatially invariant', 'ISI')

364   (**Fig. 4B**) (Methods). Classification by immune spatial lability (ISL versus ISI) was highly

365   predictive of PFS after ICB treatment (hazard ratio = 0.09, p = 0.00095), unlike classification by

366   PD-L1 using either classical NSCLC groupings – < 1%, 1-49%, $\geq$ 50% (p = 0.55) – or binary

367   cutoffs of either 1% (p = 0.27) or 50% (p = 0.77) (**Fig. 4C, Extended Data Fig. 10A**). Moreover,

368   classification by bulk expression using either all genes or 8 previously published gene sets for

369   NSCLC IO response was not predictive of PFS. However, notably a DNA damage response

370   gene set was predictive (p = 0.003) only when using SLAB scores instead of gene expression (p

371   = 0.33) (**Extended Data Fig. 10B,C**) (**Supplementary Table 3**). Moreover, eight out of the

372   twelve patients with measurable disease at treatment onset demonstrated shrinkage in tumor

373   volumes shortly after treatment began, suggesting that classification by PFS was detecting

374   differences in treatment response and durability rather than in treatment-agnostic factors such

375   as disease prognosis (**Extended Data Fig. 10D**) (Methods). Together, these results showed

376   that our pan-tumor classification schema, defined by variation in spatial lability, was sufficient to

377   distinguish variation in response to ICB therapy in our patient cohort in contrast to PD-L1 IHC

378   and previously published bulk expression gene sets.

379   Since our pan-tumor classification distinguished the NSCLC tumors as immune spatially

380   labile versus immune spatially invariant, we sought to determine which biological processes

381   were relevant to NSCLC ICB response. We tested whether genes with differential SLAB scores

382   at the pan-tumor group E branchpoint also exhibited differential SLAB scores between the ISL

383   and ISI NSCLC datasets. Of the 537 genes distinguishing the group E branchpoint, 398 were

384   also statistically enriched for spatial lability in NSCLC ISL tumors compared to NSCLC ISI

385   tumors, while the other 139 were not (**Fig. 4D, left**). Pathway analysis of these two gene groups

386   demonstrated that both groups related to immune activation and signal transduction (**Fig. 4D,**

387   **right**). However, the 139 non-differential SLAB genes were enriched for signaling via the VEGF

388   receptor, estrogen receptor, and NTRK receptors – signaling pathways implicated in immune

389   activation in cancers other than lung cancer. On the other hand, the 398 differential genes were

390   enriched for immune signaling pathways (e.g. vesicle transport) and specifically for Notch

391   signaling, a pathway that has been implicated to mediate immune checkpoint exhaustion in lung

392   cancer through a variety of mechanisms[59]. Closer investigation of the Notch pathway

393   demonstrated a set of 11 genes with coordinated SLAB changes between ISL and ISI tumors

394   (**Extended Data Fig. 11**). As an example, an examination of three genes (HDAC6, NOTCH2,

395   and PSEN1) that each promote Notch pathway activation via distinct mechanisms demonstrated

396   spatially coordinated expression changes at large, medium, and small SG scales (**Fig. 4E**).

397

398 **<u>Discussion</u>**

399   Through statistical analysis of a broad diversity of solid tumors, we have shown that there

400   is a conserved, hierarchical spatial architecture that organizes the apparent biological

401   complexity of the TME. Individual spots group together into either non-nested or nested SGs

402   which hierarchically integrate into the whole biopsy sample, thereby providing a holistic picture

403   of emergent TME organization. The results in **Figs. 3** and **4** suggest a cohesive model that

404   directly links this spatial architecture with clinical response to ICB therapy in patients. SGs are

405   information-dense units of spatial organization encoding complex molecular interactions

406   between cells and variation amongst SG-based TME profiles distinguishes ICB therapy

407   response (**Fig. 4F**, left). Our findings have implications for both tumor biology and for translation

408   towards clinical oncology.

409   With respect to tumor biology, our findings demonstrate that Spatial Groups can be

410   conceptualized as statistical 'units' of the hierarchical organization in TMEs. A natural next step

411   is to deeply interrogate the biology underlying this statistical structure to elucidate drivers of

412   variation in SG distribution and TME organization (**Fig. 4F**, top right). In general, existing

413   biological knowledge of tumors (e.g. databases reflecting experimental results from cell lines

414   and *in vivo* models) has viewed individual cells as the components of interest with respect to

415   understanding properties of whole tumors. Our results suggest an alternative foundation for

416   biological interrogation: the collective spatial interactions amongst SGs are key to understanding

417   emergent biological qualities of tumors. Elucidating the biology underlying these interactions will

418   likely require interrogating SGs without perturbing their native context rather than isolating and

419   removing them from a tumor. As such, approaches studying SG variation under observable

420   metabolic gradients and pairing SG identification with spatial metabolomics and proteomics may

421   be useful for discovering biological mechanisms influencing TME organization.

422   Efforts to bring spatial molecular profiling into clinical settings are limited by not having a

423   consensus description of tumor spatial biology. Terms such as "immune inflamed", "immune

424   excluded", and "immune desert" have served as a useful paradigm, yet, as recent studies have

425   illustrated, are too broad for describing TME heterogeneity[60,61]. Our results demonstrate how

426   treating the TME as an emergent cellular ecosystem and identifying conserved statistical

427   features of spatial organization results in a holistic, unbiased, and quantitative approach for

428   classifying tumors. The resulting SG-based classification was built on a discovery cohort of 96

429   tumors spanning twelve tumor types gathered from multiple institutions and countries and tested

430   in a validation cohort on a tumor type (NSCLC) with markedly low representation in the

431   discovery cohort. Importantly, our discovery cohort was not pre-selected to represent variation

432   in ICB response but was assembled in an unbiased manner and studied to characterize the

433   biology reflecting heterogeneity in TME spatial organization. Thus, the success of this

434   classification in delineating responders and non-responders to ICB therapy in the setting of

435   metastatic NSCLC underscores the shared qualities of SGs across tumor types and suggests

436   that variation amongst TME SG profiles may be useful for developing a framework for

437   therapeutic 'logic' (**Fig. 4F**, middle right). NSGs may have increased relevance for

438   understanding and targeting key aspects of cell-cell signaling while non-NSGs might reflect

439   elucidating molecular determinants of tumor fitness that are independent of the local

440   environment. The incorporation of more cohort studies into our classification where pre-

441   treatment biopsy samples are coupled with outcomes following therapeutic intervention will

442   address this concept. It is possible that future studies of patient cohorts in both ICB-naïve and

443   ICB-refractory settings could leverage SG-based descriptions for the discovery of therapeutics

444   that augment ICB (**Fig. 4F**, bottom right). We anticipate that describing TMEs using SGs will

445   open the possibility of creating interpretable statistical models of the TME that enable spatially

446   informed precision oncology.

Behera et al., Figure 1
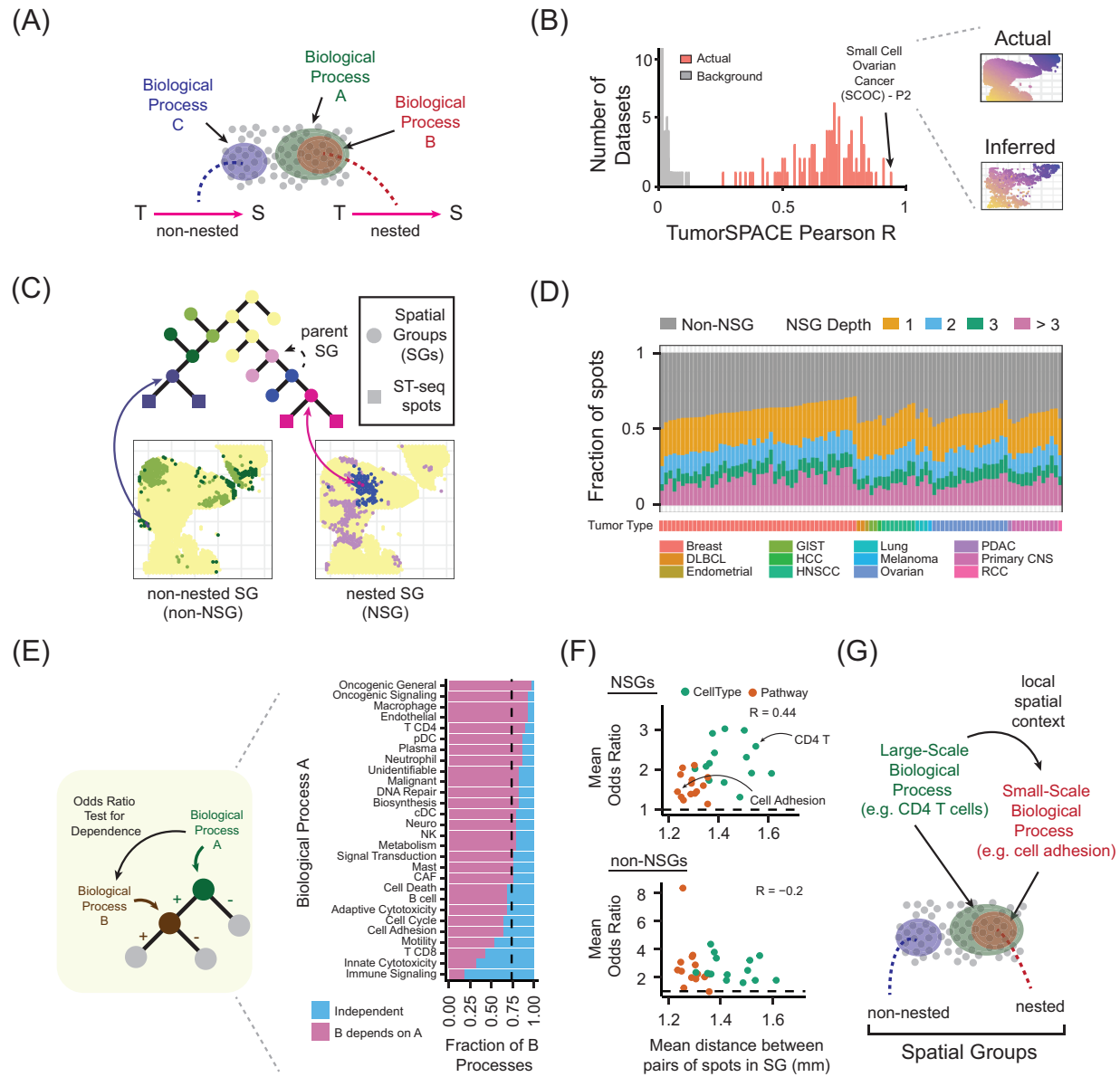
Figure 1. A conserved architecture of TME spatial biology. (A) A map (pink arrows) relating transcriptional ('T') and spatial ('S') information that captures non-nested and nested spatial contexts of biological processes. **(B)** Histogram of correlation values (Pearson R) between actual spatial distances for all pairs of spots within a given ST-seq dataset and pairwise distances inferred by TumorSPACE. Gray distribution reflects a background expectation of correlation values (Methods). (Inset) Actual spot locations and inferred spot locations for the small-cell ovarian cancer patient 2 ST-seq dataset (SCOC-P2). **(C)** (Top) Section of TumorSPACE map for sample SCOC-P2; squares at the bottom of the tree are individual spots, each circle is a Spatial Group (SG). 'Parent SG' is delineated to define the relationship between SGs. (Bottom) Picture of actual SCOC-P2 spot locations with spots colored by SG designation. The left and right panels illustrate examples of non-nested spatial groups (non-NSGs) and nested spatial groups (NSGs) respectively. **(D)** Fraction of spots in an ST-seq dataset (y-axis) belonging to non-NSGs (gray bars) or NSGs of varying depth (colored bars) for all tumors in our pan-tumor database ('Tumor

461 Type' on x-axis, see color key). **(E)** (Left) Workflow for evaluating if a differentially abundant
462 biological process within a parent SG ('Biological Process A') influences a biological process
463 within an NSG ('Biological Process B'). (Right) The fraction of processes in an NSG (x-axis) that
464 are dependent (purple bar) or independent (blue bar) on processes in a parent SG (y-axis). **(F)**
465 Mean odds ratio (y-axis) of processes (colored dots) versus size of SG (x-axis). **(G)** A model of
466 TME spatial biology: TMEs are comprised of non-nested and nested Spatial Groups. Nested
467 spatial groups encode large-scale processes that influence small-scale processes.
468

Behera et al., Figure 2
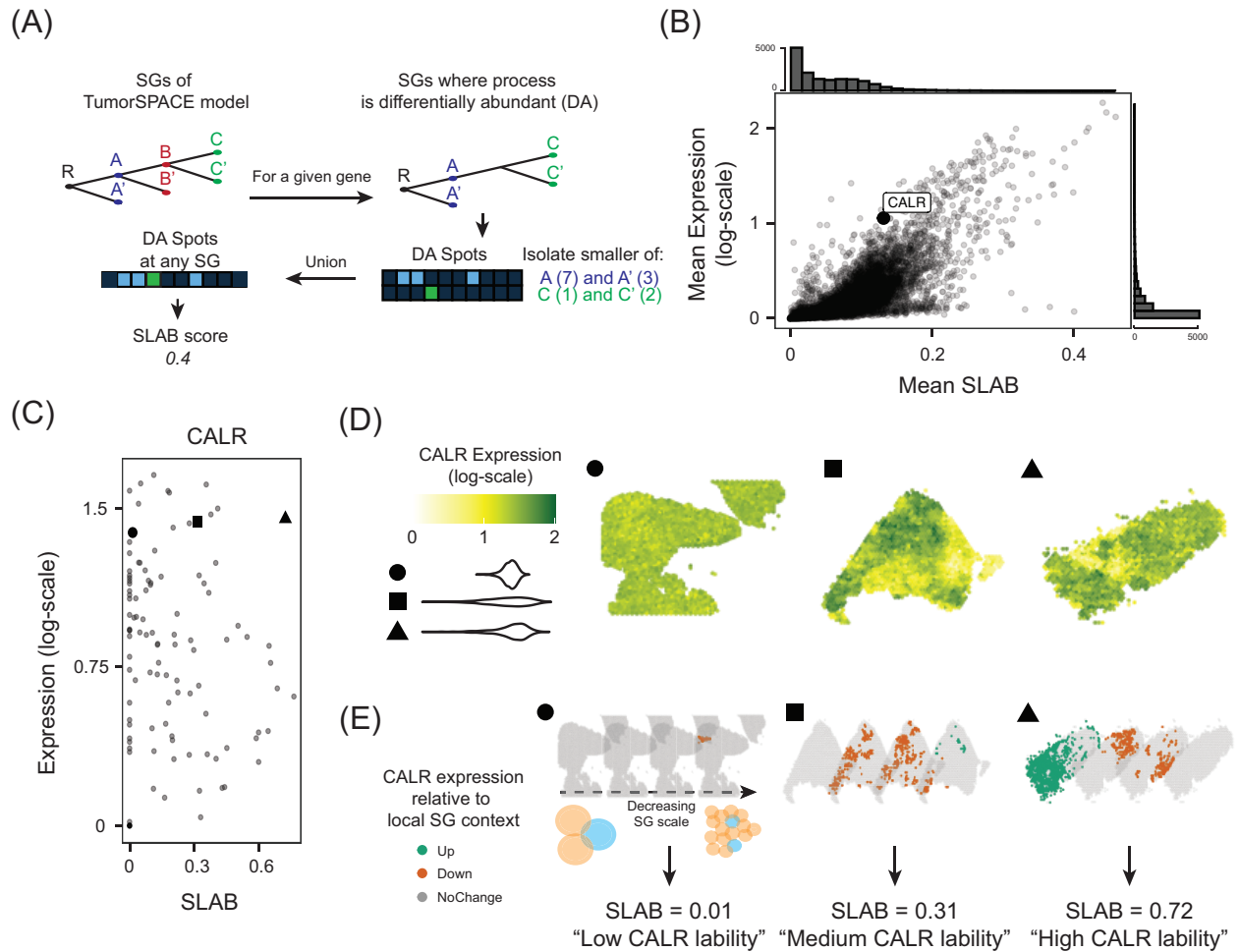
Figure 2. Spatial lability: a measure of spatial heterogeneity based on Spatial Groups. (A) Workflow for computing spatial lability (SLAB) score. R is the root SG in this example dataset consisting of 10 spots and 6 descendant SGs: A, A', B, B', C, C'. Highlighted spots reflect spots belonging to the smaller of the descendant SGs from R (Methods). Numbers in parentheses indicate number of spots within an SG. **(B)** Mean gene expression for all genes across all tumors in our database (y-axis) versus mean SLAB score across all tumors in our database (x-axis). Each point is a single gene; density of points enumerated by histograms on x and y axes. Dot in the center is the gene calreticulin (CALR). **(C)** Expression of CALR averaged across all spots in each tumor (y-axis) versus CALR SLAB score (x-axis). Each dot is a tumor in our database. Three tumors (black circle, square, and triangle) are highlighted that harbor the same mean CALR expression but varying SLAB scores. **(D)** Spatial distribution of CALR expression across tumors highlighted in panel C. CALR expression is represented in log-scale (see colorbar); below colorbar is distribution of CALR expression across all spots in the labeled tumor. Spots in each triangle, square, and circle tumors are colored by CALR expression. **(E)** CALR expression within SGs illustrated as SGs decrease in spatial scale for circle, square, and triangle tumors with corresponding spatial lability scores. Green spots reflect increased CALR expression within SG; brown spots reflect decreased CALR expression within SG; gray spots reflect no difference in expression within SG. SGs are included in plots from left to right if they impact (i) 20 – 50% of

489   biopsy spots, (ii) 10 – 20% of biopsy spots, (iii) 5 – 10% of biopsy spots, or (iv) less than 5% of
490   biopsy spots. SLAB scores are computed from the union of colored spots and displayed below.
491

Behera et al., Figure 3
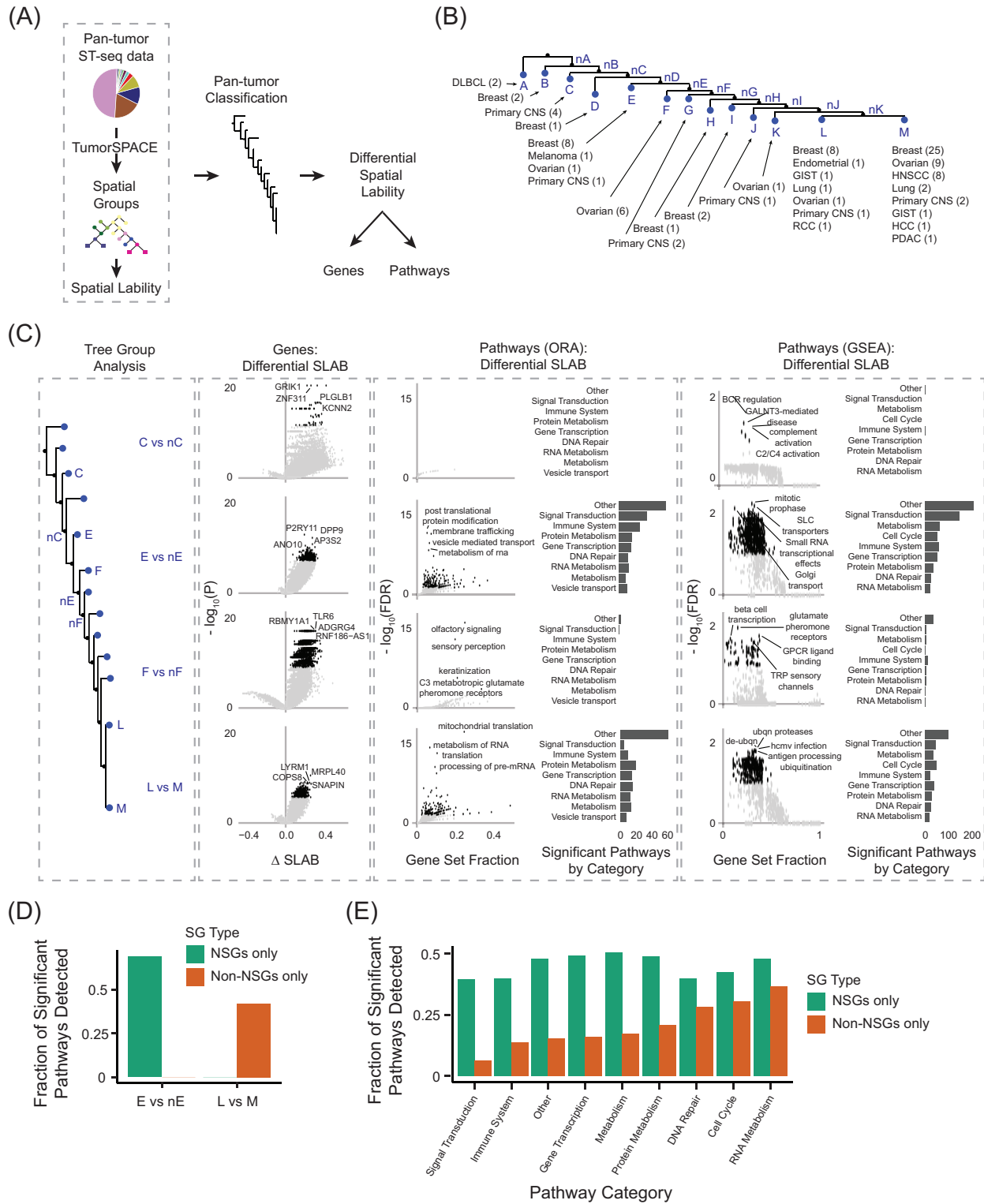
495 **Figure 3. Pan-tumor spatial lability classification distinguishes tumors by spatial**
496 **heterogeneity amongst cell-intrinsic and cell-extrinsic processes. (A)** Workflow for defining
497 and interrogating a classification of tumors based on spatial lability. **(B)** The pan-tumor
498 classification tree. Each leaf is labeled alphabetically and comprised of specific tumors with the
499 remaining tumors labeled to indicate not being a part of the group of tumors in the leaf. For
500 instance, two Diffuse Large B Cell Lymphoma (DLBCL) tumors comprise group A; all other tumors
501 comprise the 'nA' category. Parentheses indicate number of tumors of a specific tumor type in the
502 group. **(C)** (Left) Branchpoints in the spatial lability classification where any statistically significant
503 differences in gene spatial lability were detected. (Middle) Volcano plots describing significant
504 differences in gene spatial lability for each group. (Right) Over-representation analysis (ORA) and
505 gene-set enrichment analysis (GSEA) of pathway-based spatial lability. Within each sub-panel
506 (ORA, GSEA), these results are shown as Volcano plots and histograms grouped by pathway
507 category. **(D)** Fraction of significant pathways detected by GSEA (see **Fig. 3C**, right) that were
508 enriched (y-axis) at branchpoints E vs nE or L vs M (x-axis) when considering spots within only
509 NSGs (green) or only non-NSGs (orange). **(E)** Fraction of significant pathways per pathway
510 category detected by GSEA (see **Fig. 3C**, right; x-axis) that were enriched at any branchpoint (y-
511 axis) when considering spots within only NSGs (green) or only non-NSGs (orange).
512
513

Behera et al., Figure 4
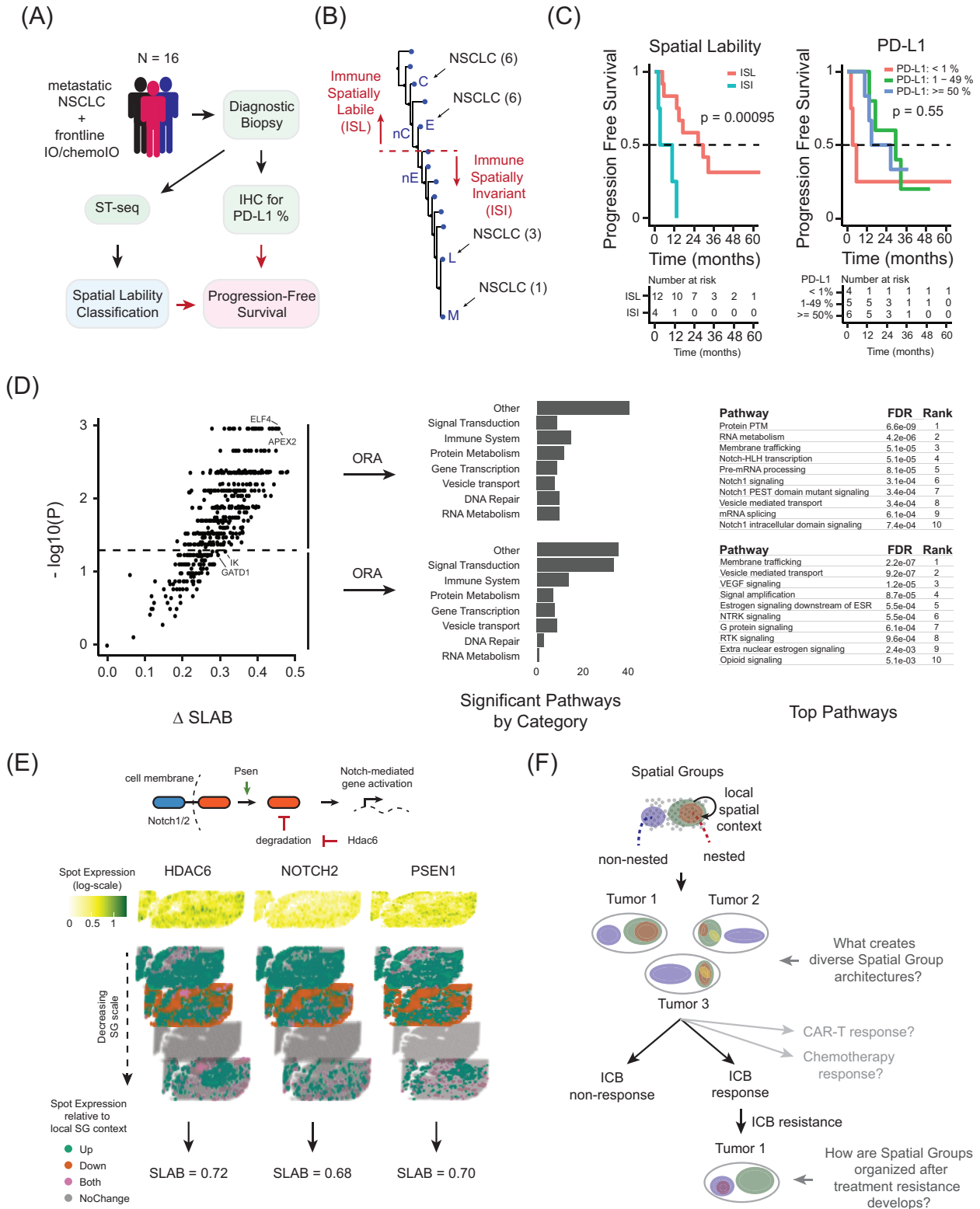
516 **Figure 4. Pan-tumor classification distinguishes responders to immune checkpoint**
517 **blockade in metastatic non-small cell lung cancer (NSCLC). (A)** Sixteen patients with
518 metastatic NSCLC underwent a diagnostic biopsy and were given immunotherapy (IO) or a
519 combination of IO and chemotherapy. The diagnostic biopsy was subjected to ST-seq and
520 immunohistochemistry (IHC) for PD-L1 status. From the ST-seq data, spatial lability classification
521 was performed, and progression-free survival (PFS) was compared between groups defined by
522 (i) spatial lability and (ii) PD-L1 status. **(B)** Comparison of NSCLC samples from panel A with the
523 pan-tumor classification from **Fig. 3B**. Twelve samples had similar spatial lability profiles to tumors
524 in groups C and E ('Immune Spatially Labile', 'ISL'). Four samples had similar spatial lability
525 profiles to tumors in groups L and M ('Immune Spatially Invariant', 'ISI'). **(C)** Kaplan-Meier curves
526 for PFS (y-axis) in months (x-axis) stratified by ISL/ISI (left) or by PD-L1 status (right). Number at
527 risk tables show the number of patients remaining uncensored at each time point. **(D)** SLAB
528 scores amongst the 537 genes defining the branchpoint of group E versus nE in **Fig. 3B** were
529 computed for all NSCLC tumors. (Left) Volcano plot depicts difference in spatial lability (x-axis)
530 and Wilcoxon p-value (y-axis, log-transformed) for NSCLC tumors grouped by ISL versus ISI.
531 Dashed line indicates p = 0.05. Over-representation analysis (ORA) of the 537 genes stratified by
532 p <= 0.05 (upper) or p > 0.05 (lower) is represented as number of significant pathways grouped
533 by category (Middle) and top pathways (Right). **(E)** Part of the NOTCH signaling cascade (top
534 panel) highlighting three proteins: NOTCH2, PSEN1, and HDAC6. Gene expression of these
535 three proteins across an NSCLC sample (colorbar in white to green); gene expression changes
536 of these three proteins in the depicted NSCLC sample across SGs (bottom panel with associated
537 color key). **(F)** A depiction of our model that relates tumor SG profiles to NSCLC ICB response
538 (left) and future directions motivated by these results (right).
539

Behera et al., Extended Data Figure 1
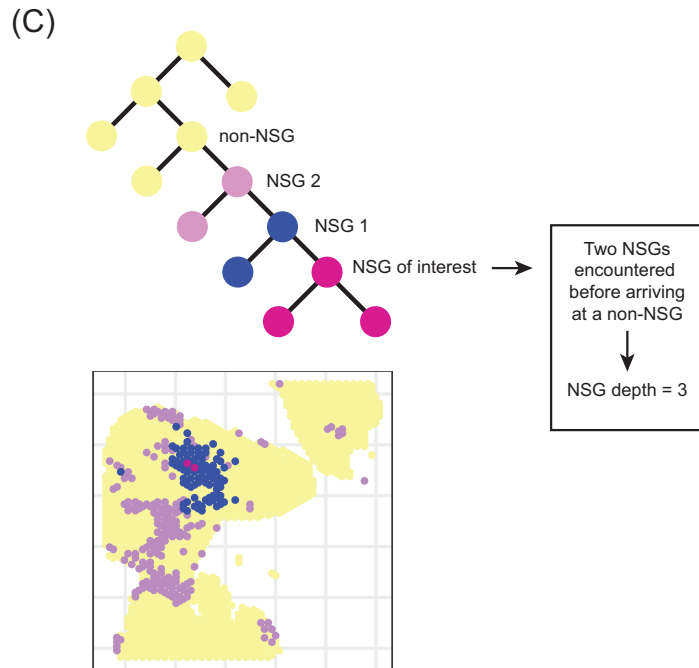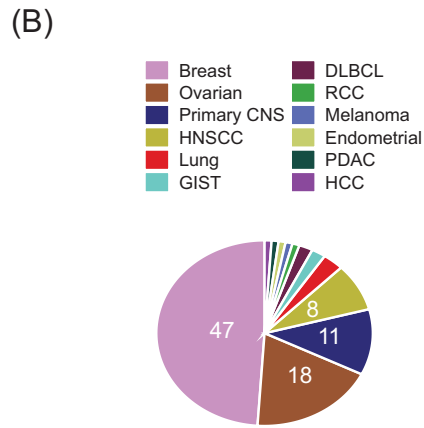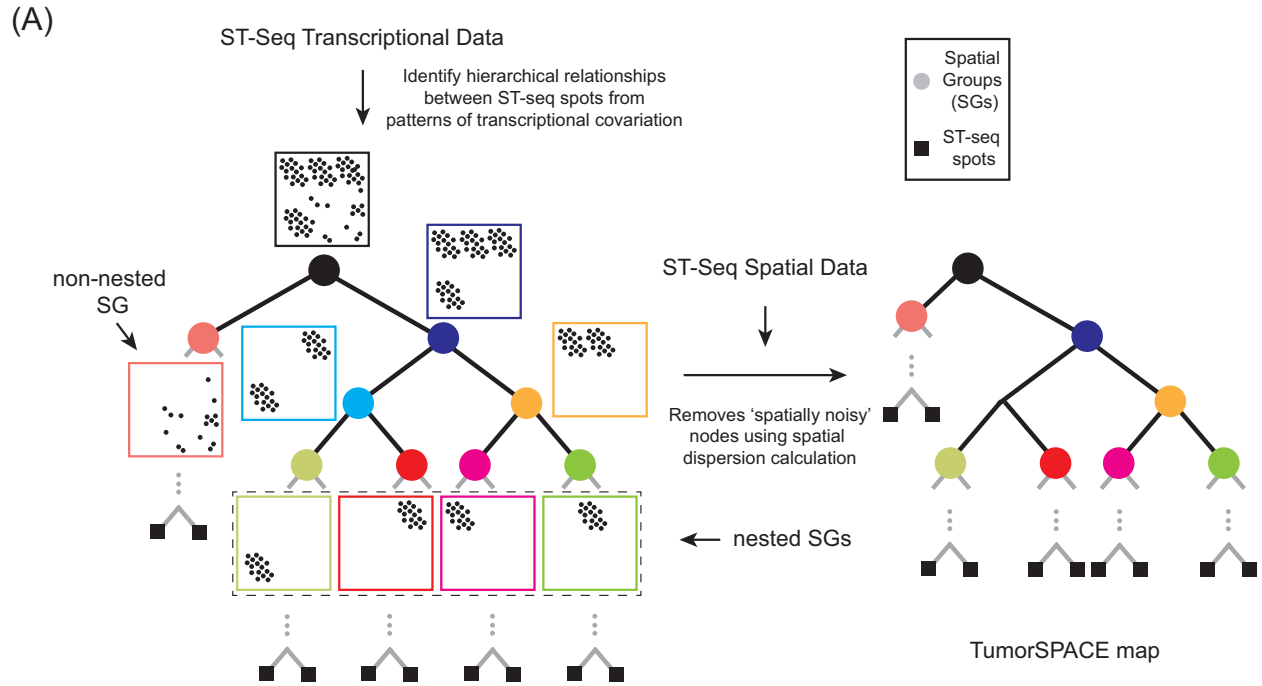

540
541
542
543
544
545

546 **Extended Data Figure 1. (A)** Workflow for generating a TumorSPACE map involves first
547 identifying hierarchical relationships between ST-seq spots using transcriptional data alone (left)
548 and then performing 'spatial de-noising' by removing tree nodes with high spatial dispersion
549 values (right) (Methods). These maps can capture both spatially nested and spatially non-nested
550 spot relationships. Grey lines at the bottom of each branchpoint indicate that trees continue to
551 branch until terminating at the individual ST-seq spots (black squares). **(B)** Description of our pan-
552 tumor ST-seq database. Number of datasets for each tumor type (color key) is delineated in the
553 pie graph. **(C)** Description of how NSG depth is calculated for an example set of SGs.
554

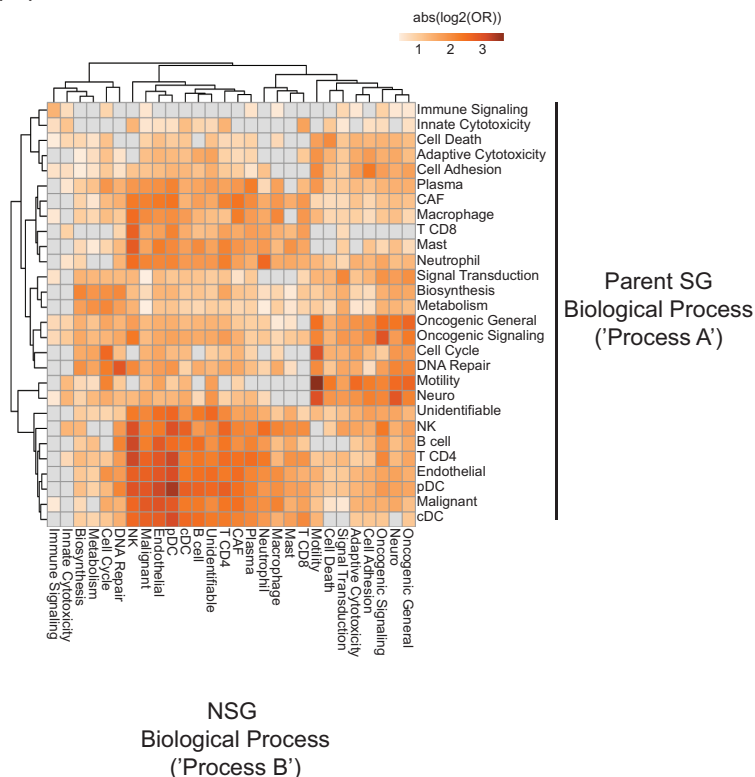Behera et al., Extended Data Figure 2
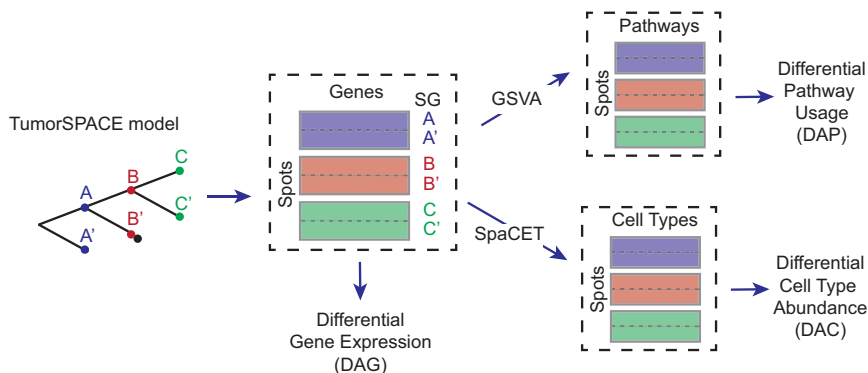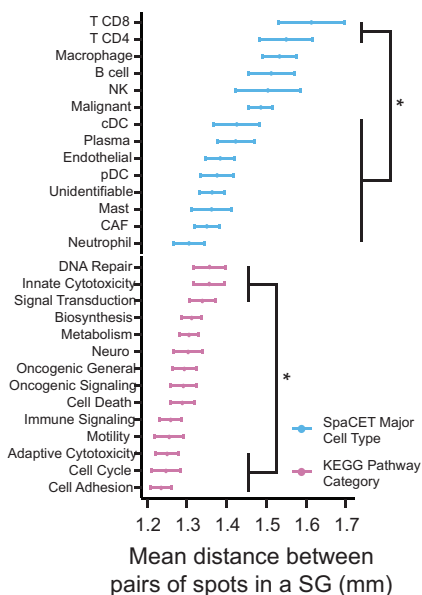
555
556
557   **Extended Data Figure 2. (A)** Using TumorSPACE models to conduct differential analysis of gene
558   expression, pathway usage with gene set variation analysis (GSVA), and cell type differences
559   using SpaCET for spot deconvolution into cells[39]. SGs are labeled as A, A', B, B', C, and C'. **(B)**
560   Mean distance between pairs of spots within a SG across SGs for all ST-seq datasets in our
561   database (x-axis) versus all KEGG pathway categories (purple) and all major cell types as defined
562   by SpaCET (blue) (y-axis). Error bars reflect 95% confidence intervals. *Wilcoxon p-value < 1e-
563   9. **(C)** Odds ratio (absolute value, log-scaled) that a parent SG biological process ('A', rows) is
564   associated with a coordinated direction of change in a second biological process ('B', columns)

565   reflected within a daughter NSG. Color key indicates magnitude of effect where 1 indicates no
566   effect. Gray cells indicate biological process pairs that were not observed. Rows and columns are
567   hierarchically clustered.
568

Behera et al., Extended Data Figure 3
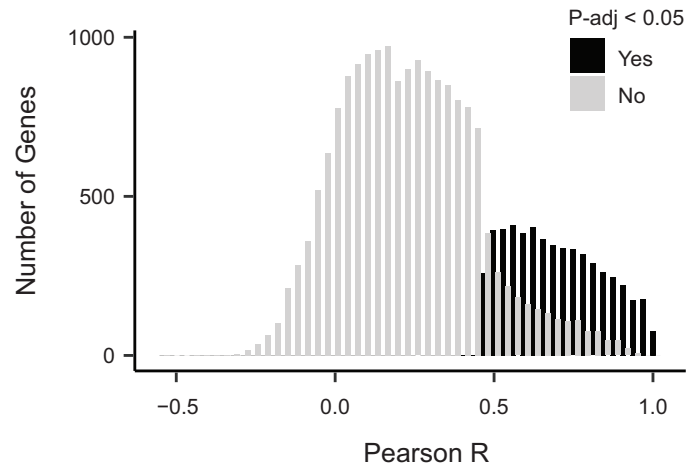
Extended Data Figure 3. Histogram of correlations (Pearson R) between bulk gene expression and SLAB scores across all tumors in our pan-tumor database for all genes. Genes are stratified by whether correlation was statistically significant (black) or not (grey) compared to an empirical null distribution.

Behera et al., Extended Data Figure 4
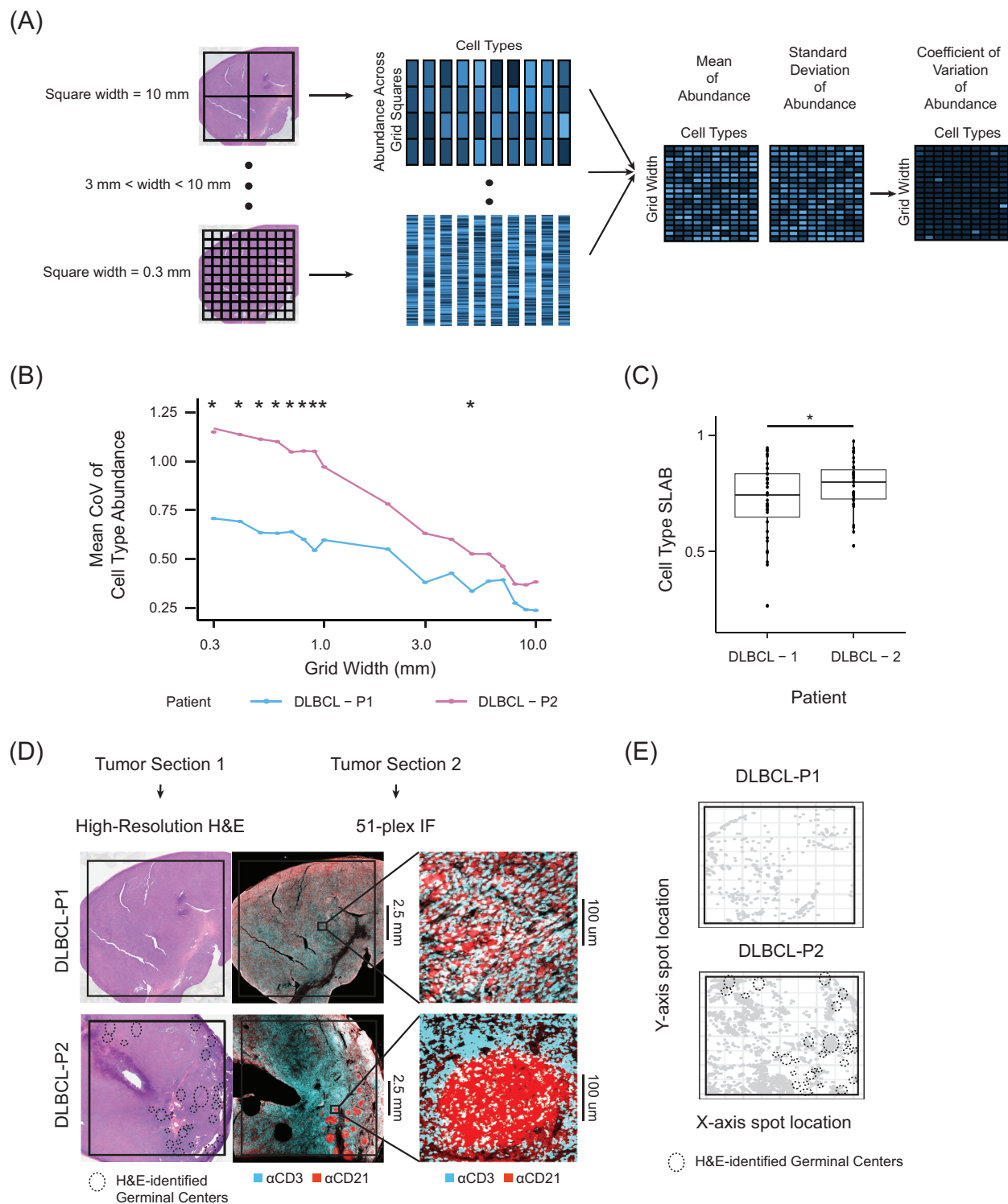
Extended Data Figure 4. (A) Schematic for computing the coefficient of variation (CoV) for cell type abundance across a slide from immunofluorescence (IF) data. **(B)** Mean CoV across all cell types (y-axis) versus grid width of biopsy region (x-axis) for DLBCL-P1 (blue) and DLBCL-

581   P2 (purple). (* Wilcoxon p < 0.05) **(C)** Distribution of SLAB scores (y-axis) for cell types (y-axis)
582   in DLBCL-P1 and DLBCL-P2 (x-axis). **(D)** High-resolution H&E (left) and 51-plex IF (right)
583   images for DLBCL Patients 1 (top) and 2 (bottom). Colors in IF images represent staining for T
584   cells (anti-CD3, blue) and B cells (anti-CD21, red). **(E)** Spatial distribution of spots (grey dots) in
585   DLBCL-P1 (upper) and DLBCL-P2 (lower) within SGs with simultaneous B cell enrichment and
586   T cell depletion. **(D, E)** Dashed circles indicate germinal centers identified from the
587   corresponding H&E images.
588

Behera et al., Extended Data Figure 5
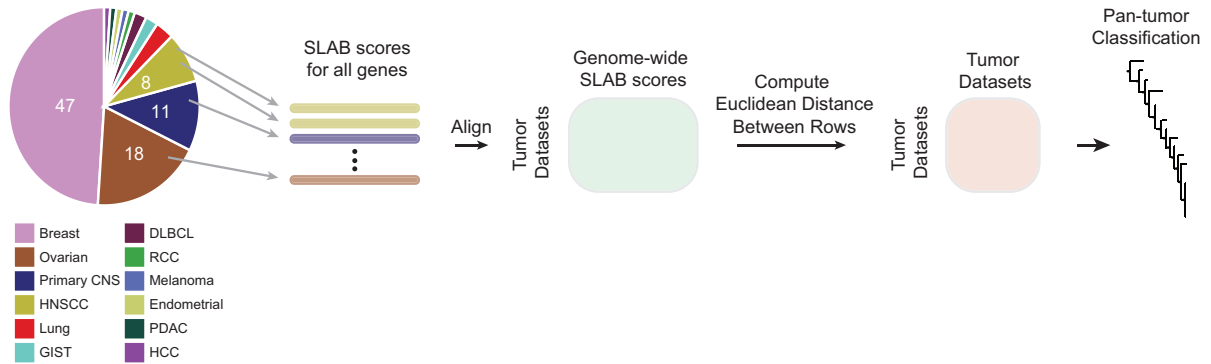
Extended Data Figure 5. Workflow for pan-tumor classification by SLAB scores. First, SLAB scores are computed for each gene for all tumors. This creates a genome-wide profile of SLAB scores for each ST-seq dataset. The datasets are aligned by their genome-wide SLAB profiles creating a matrix where rows are ST-seq datasets, columns are genes, and each entry is the SLAB score for a gene in an ST-seq dataset. Euclidean distance based on genome-wide SLAB scores is computed for all pairs of ST-seq datasets. Hierarchical clustering of pairwise SLAB-based distance results in a pan-tumor classification where tumors that are close together share a similar genome-wide SLAB profile.
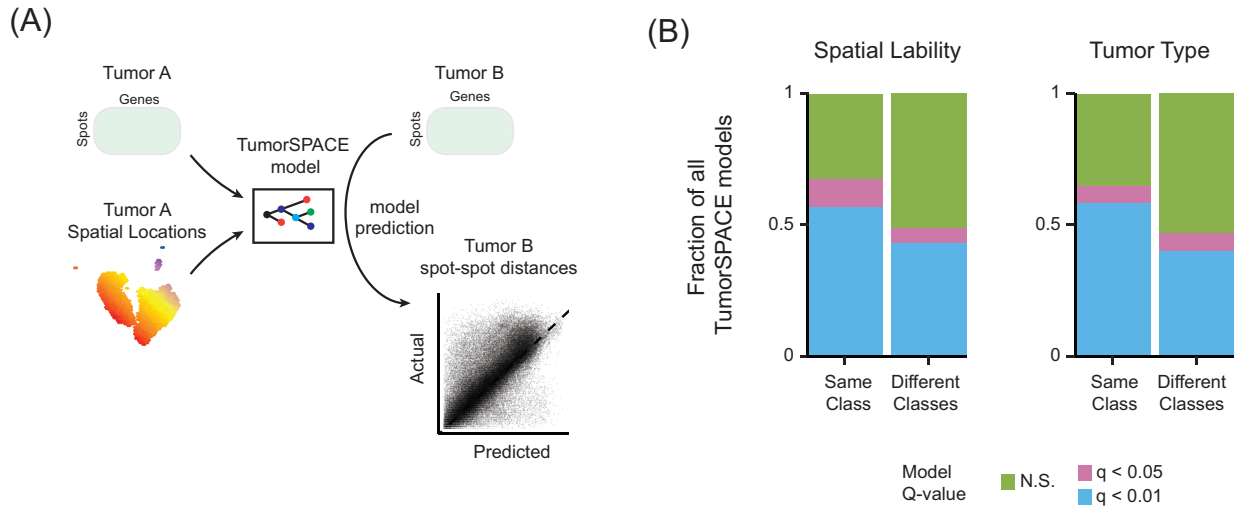
Behera et al., Extended Data Figure 6

(A)

(B)
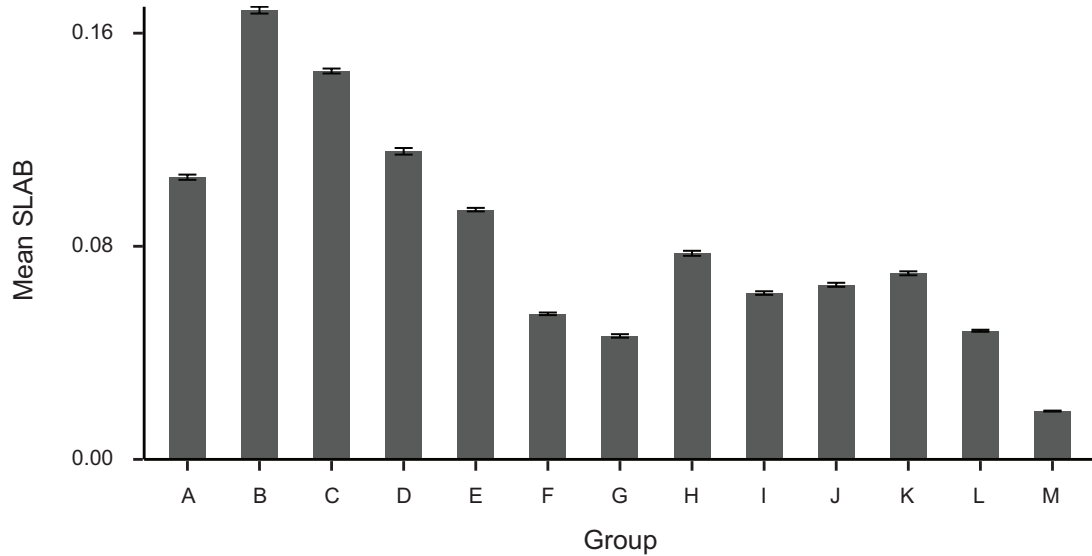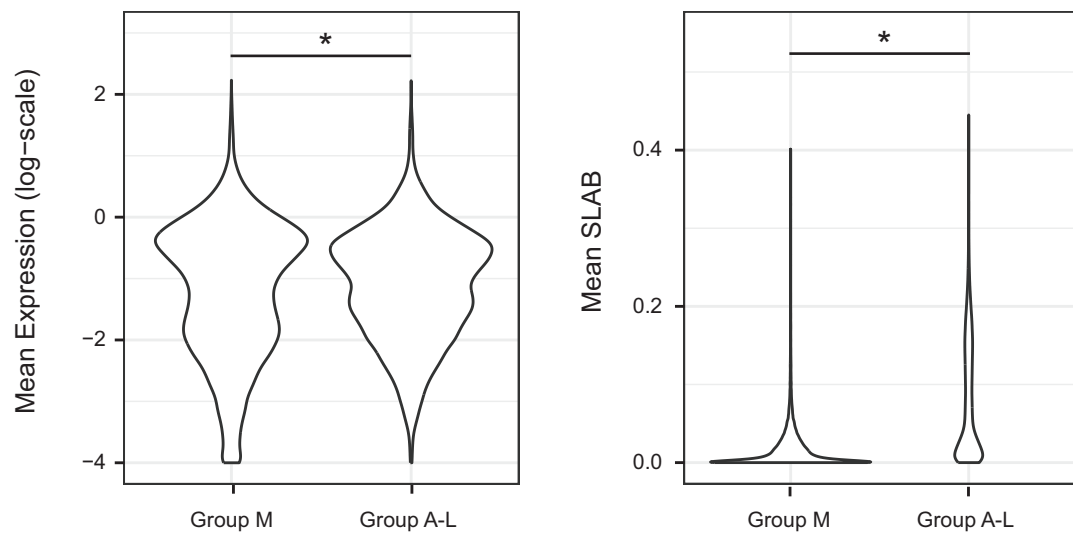
Extended Data Figure 6. (A) First, for a given gene, the mean SLAB score is computed grouped by spatial lability as in **Fig. 3B** (x-axis). Second, the mean of these group-wise SLAB scores was computed across all genes (y-axis). Error bars depict standard error of the mean. **(B)** Violin plots depicting mean gene expression (log-scale, left) and mean SLAB (right) for all genes where tumors in the pan-tumor database were grouped by whether they belonged to Group M or Groups A-L. * Paired Wilcoxon p < 1e-100.

Behera et al., Extended Data Figure 7

(A)

(B)

(C)

$$[A:B\ Prediction]\ \sim N(Intercept + \beta_1*TumorType + \beta_2*SpatialLabilityType)$$

Coefficient	Estimate	Std. Error	Pr(>|t|)
Intercept	0.072325	0.002326	< 2e-16
Tumor Type = Same	0.034787	0.004307	1.09e-15
Spatial Lability Class = Same	0.034831	0.005313	6.92e-11

609
610
611 **Extended Data Figure 7. (A)** Workflow for testing if a TumorSPACE model built for tumor A could
612 predict the spatial organization of tumor B. **(B)** Proportion of all pairs of non-Group M
613 TumorSPACE models that are predictive for spot-spot distances (y-axis) when pairs are stratified
614 as being within the same class or different classes (x-axis). Classes were defined by either spatial
615 lability (left) or by tumor type (right). **(C)** Linear modeling of cross-tumor spatial prediction using
616 either tumor type or spatial lability class as independent variables.
617

Behera et al., Extended Data Figure 8

(A)

(B)
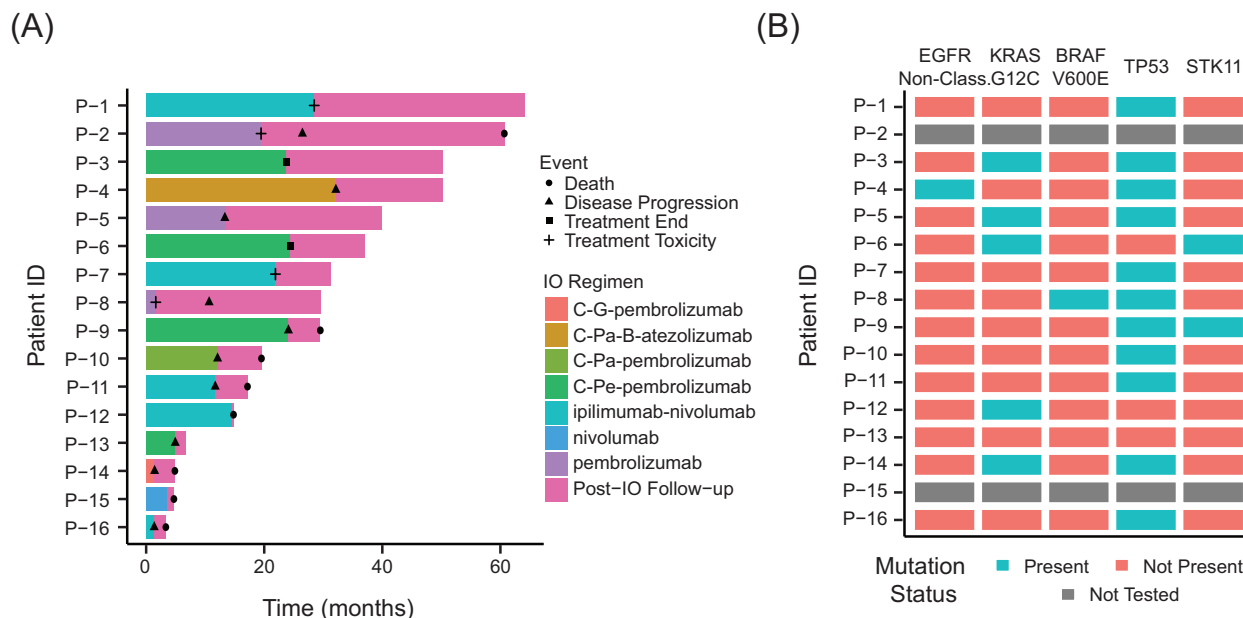
(C)

Characteristic	HR[1]	95% CI[1]	p-value
RegimenType			
ChemoICB	—	—	
MonoICB	2.78	0.67, 11.5	0.2
DualICB	0.92	0.22, 3.91	>0.9
KRAS_G12C			
N	—	—	
Y	0.70	0.19, 2.60	0.6

[1] HR = Hazard Ratio, CI = Confidence Interval

Extended Data Figure 8. (A) Swimmer plot illustrating patient treatment courses starting when patients began frontline immunotherapy treatment in the metastatic NSCLC setting. Colors indicate immunotherapy (IO)/chemo-IO regimen, shapes indicate significant events. Chemotherapies are abbreviated as follows: C = carboplatin, G = gemcitabine, Pa = paclitaxel, B = bevacizumab, Pe = pemetrexed. IO therapies include anti-PD1 (pembrolizumab, nivolumab), anti-PD-L1 (atezolizumab), and anti-CTLA-4 (ipilimumab) therapies. **(B)** Mutation status for clinically relevant mutations amongst the 16-patient cohort at the time of pre-treatment diagnostic

627   biopsy. **(C)** Univariate analysis between (i) ICB regimen type, and (ii) KRAS G12C status and
628   progression-free survival (PFS).
629
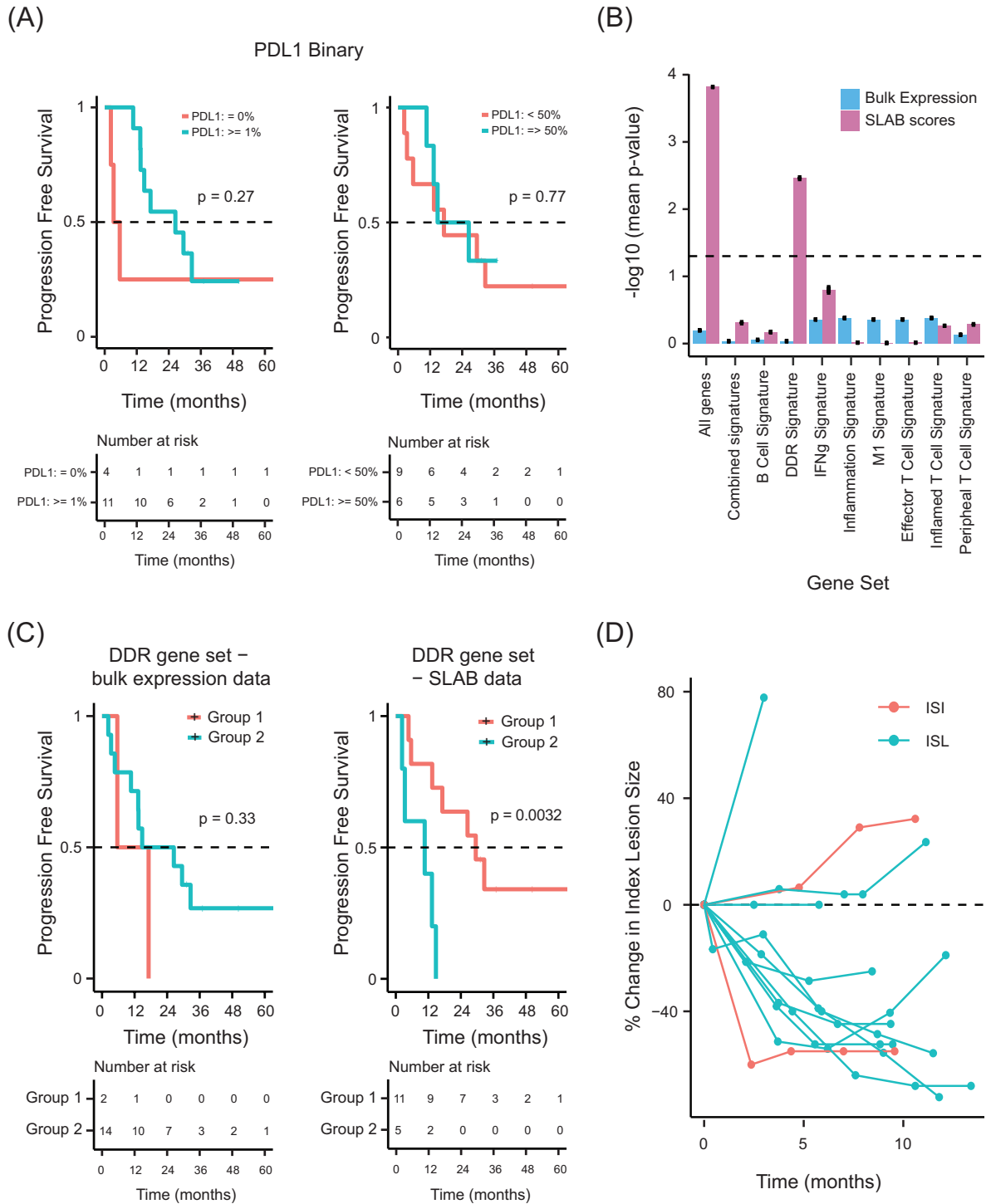
Behera et al., Extended Data Figure 9
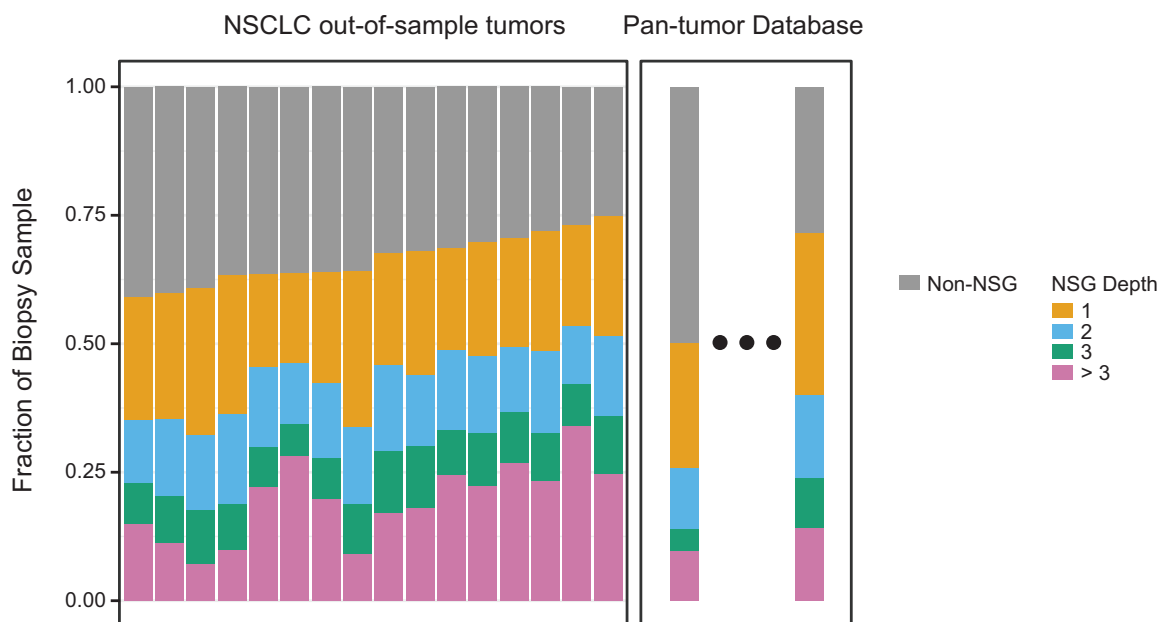
Extended Data Figure 9. Fraction of spots in an ST-seq dataset (y-axis) belonging to non-NSGs (gray bars) or NSGs of varying depth (colored bars) for NSCLC out-of-sample tumors (left) and for the two tumors in our pan-tumor database representing the highest and lowest non-NSG fraction (right).

Behera et al., Extended Data Figure 10


Extended Data Figure 10. (A) Kaplan-Meier curve of progression-free survival comparing NSCLC patients of PD-L1 status with binary cutoffs of either 1% (left) or 50% (right) by IHC. (**B**) Mean p-values (log10-transformed, y-axis) of log rank statistical tests using several gene sets (x-axis) to predict progression-free survival amongst NSCLC patients using either bulk gene

643   expression data (blue) or SLAB score data (purple) (see **Supplementary Table 3** for gene sets).
644   Error bars represent standard error of the mean when performing classification 100 times
645   (Methods). Dashed line indicates p = 0.05. (**C**) Kaplan-Meier curve of progression-free survival
646   comparing NSCLC patients stratified by the DNA Damage Response gene set using either bulk
647   expression data (left) or SLAB score data (right). (**D**) Spider plot depicting percent change in
648   volume of index tumor lesion using serial computed tomography (CT) scans (y-axis) in the months
649   following treatment start (x-axis). Each line describes a single patient classified as either ISL
650   (blue) or ISI (red), and each point on a line indicates a CT scan measurement at that time.
651

Behera et al., Extended Data Figure 11
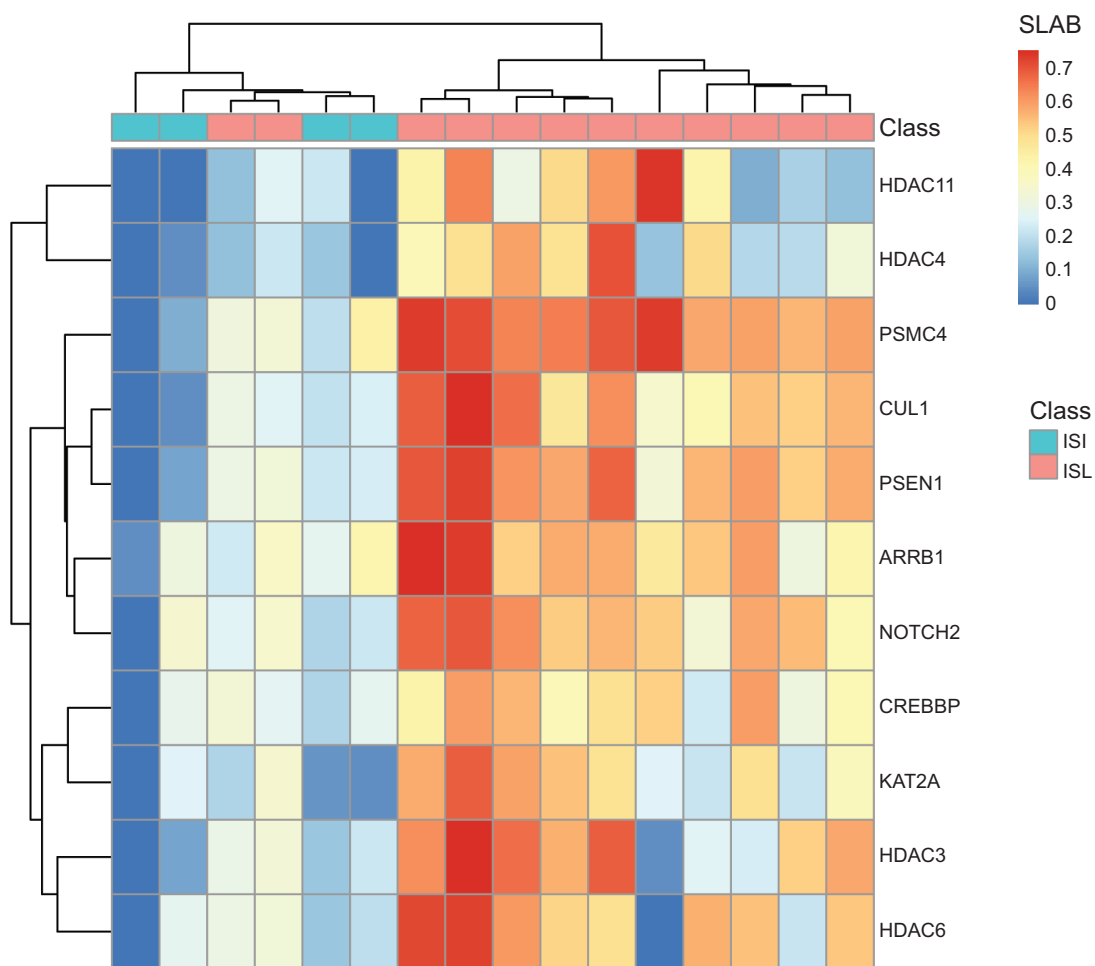
652
653
654 **Extended Data Figure 11.** Heatmap of SLAB scores (cells, see color key) for 11 NOTCH-
655 pathway genes (rows) in the 16 NSCLC datasets (columns). Both rows and columns are
656 hierarchically clustered by Euclidean Distance. Patients are labeled as either immune spatially
657 labile (ISL, red) or immune spatially invariant (ISI, blue).
658

Behera et al., Extended Data Figure 12
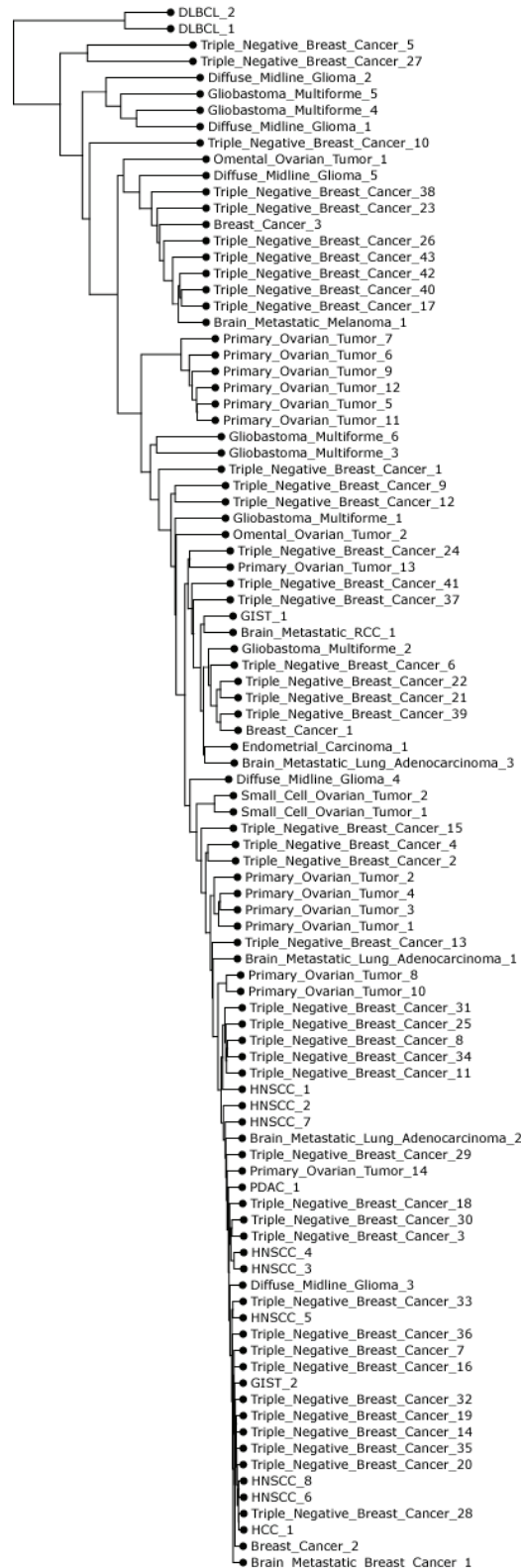
660 **Extended Data Figure 12.** Pan-tumor dataset classification by SLAB scores. Each leaf in the tree
661 is a distinct patient dataset.
662

Behera et al., Extended Data Figure 13

(A)

(B)
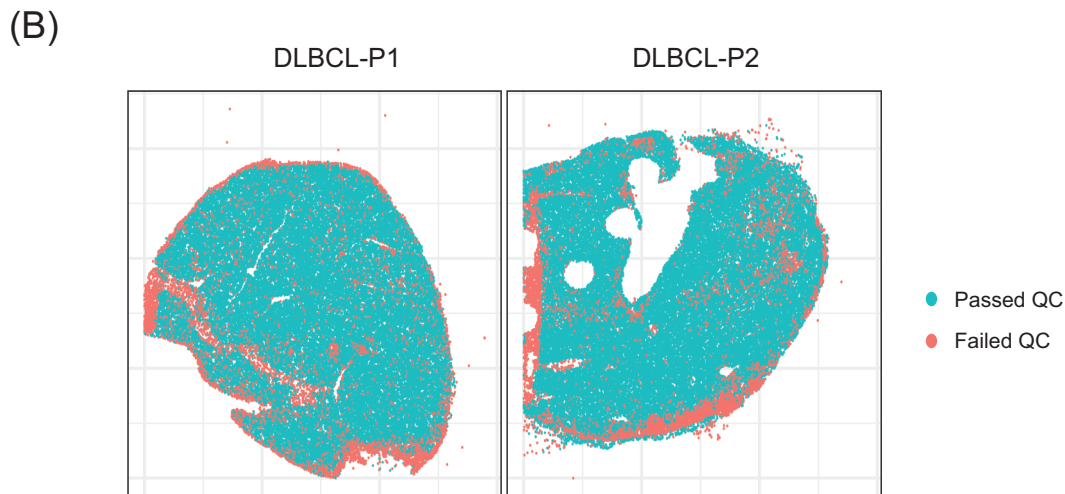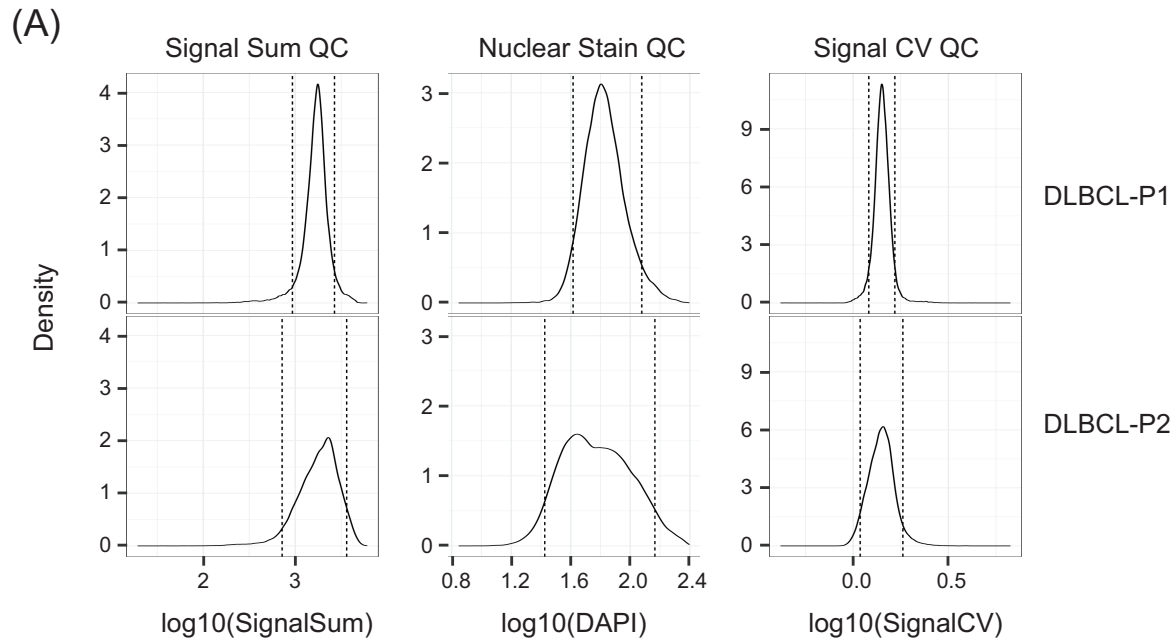
663
664
665 **Extended Data Figure 13. (A)** Density plots of QC metrics – signal sum across IF markers, signal
666 coefficient of variation (CV) across IF markers, and DAPI intensity – for DLBCL Patients 1 (top)
667 and 2 (bottom). Dotted lines represent 95% (right) and 5% (left) quantile boundaries used to
668 remove outlier cells. **(B)** Spatial locations of spots that passed (green) versus failed (red) the QC
669 thresholds in **(A)**.
670

Behera et al., Extended Data Figure 14

(A)

(B)

(C)

671
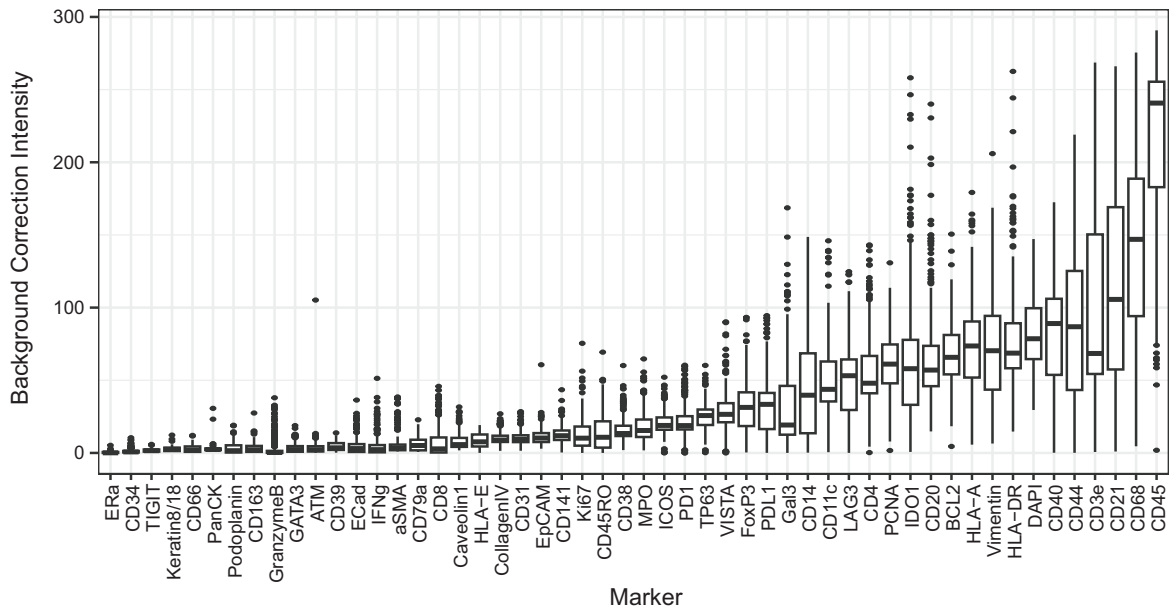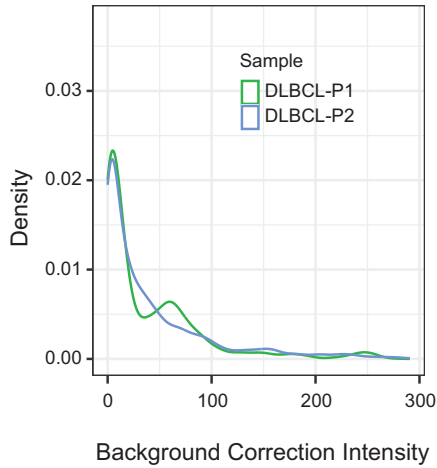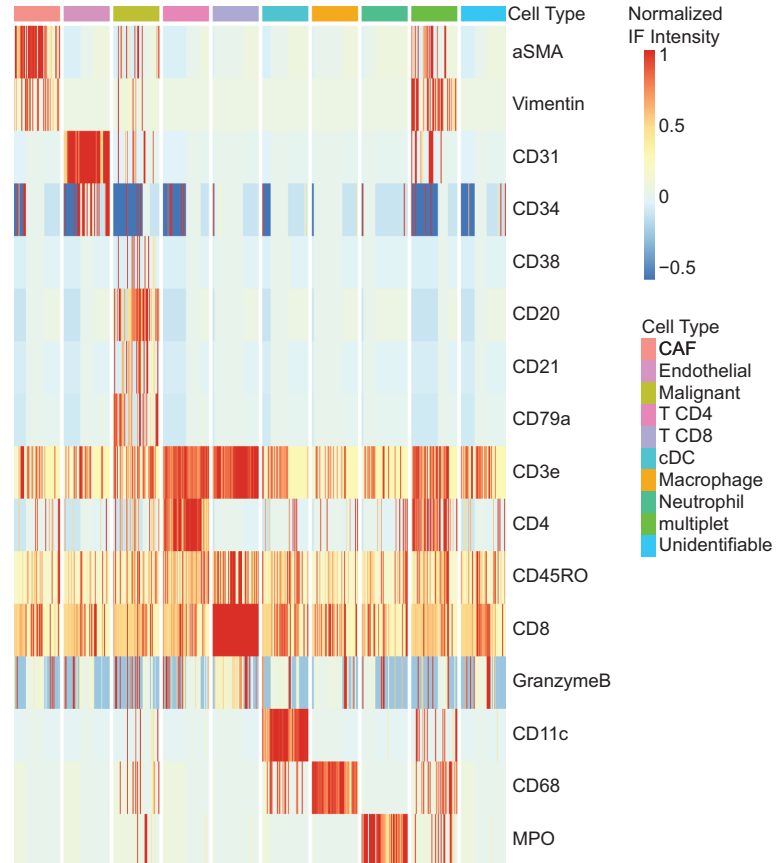
672 **Extended Data Figure 14. (A)** Background correction intensities (y-axis) for specific IF markers
673 (x-axis). Each boxplot comprises the set of region-specific intensities where each point is the
674 background correction intensity for a given tumor region. **(B)** Density plot of background correction
675 values from (A) for DLBCL Patient 1 (green) and 2 (blue). **(C)** Heatmap depicting normalized
676 intensities for representative markers (rows) from 50 cells (columns) in each cell type
677 classification group (see color key).
678

Behera et al., Extended Data Figure 15
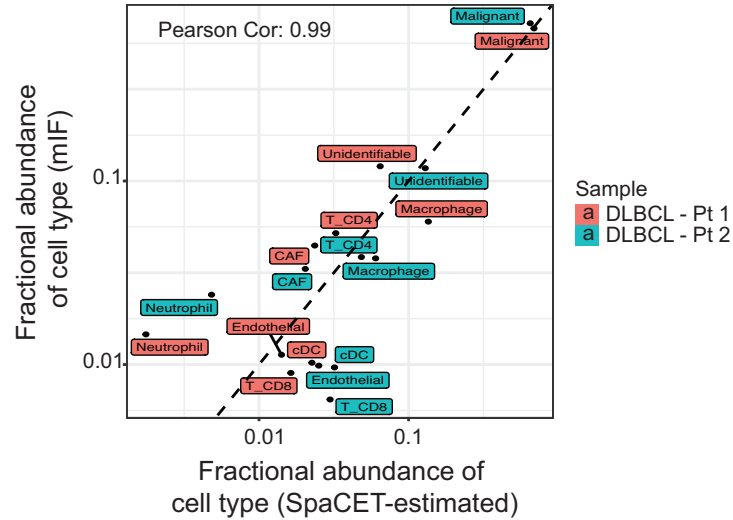
679
680
681 **Extended Data Figure 15.** Fraction abundance of cell type as determined by multiplexed
682 immunofluorescence (mIF) (y-axis) versus fraction abundance of cell type as determined by
683 SpaCET-estimated deconvolution from ST-seq transcriptional data (x-axis) for two DLBCL
684 patients shown in **Extended Data Fig. 4**. Dashed line indicates linear with associated Pearson
685 correlation.
686
687
688

689   **Methods**

690   **Computational method details**
691
692   **ST-seq dataset download and alignment**
693   Previously deposited ST-seq datasets (**Supplementary Table 1**) were downloaded for
694   integration from GEO (https://www.ncbi.nlm.nih.gov/geo/) into the pan-tumor ST-seq database
695   as long as they had the following SpaceRanger outputs available: 1) a spot-by-UMI gene count
696   matrix, 2) a spot-by-pixel location matrix, and 3) a scalefactors_json.json file containing
697   'spot_diameter_fullres'. For analyses including physical distance rather than pixel distance, pixel
698   distance was converted to physical distance by computing a $\frac{pixel}{\mu m} = \frac{\text{'spot\_diameter\_fullres'}}{55}$ scaling
699   factor that compares spot diameter in pixels to the known spot diameter of 55 μm.
700
701   **SpaceRanger**
702   For internally generated ST-seq datasets, reads were aligned and mapped to the hg38
703   (GRCh38) human genome reference using the SpaceRanger v2.0.0 count pipeline
704   (**Supplementary Table 4**). This pipeline generates a raw unique molecular identifier (UMI) gene
705   count matrix in which each row consists of a spot that has X/Y coordinates in pixels that
706   correspond to the aligned H&E image. The SpaceRanger algorithm also identifies spots within
707   or outside of detectable tissue, and for all subsequent analyses only spots within tissue were
708   used.
709
710   **TumorSPACE: models and associated analysis**
711   The sub-sections within this section will introduce a number of variables. As such, below is a
712   table of variable definitions.
713

Variable	Definition	Section Where First Referenced
M	SpaceRanger UMI gene count matrix	*Creating a latent space*
m	Number of ST-seq spots in M	*Creating a latent space*
n	Number of genes in M	*Creating a latent space*
U	SVD left singular matrix	*Creating a latent space*
Σ	SVD singular value matrix	*Creating a latent space*
V^T	Transpose of SVD right singular matrix	*Creating a latent space*
D	Spectral Distance matrix	*Creating a latent space*
p	PC depth hyperparameter	*Creating a latent space*
T	TumorSPACE tree model	*Creating a latent space*
G	The set of tree internal nodes	*Creating a latent space*
g	A single tree internal node	*Creating a latent space*
M_B	Bootstrapped gene count matrix	*Bootstrapping the latent space…*
X	Statistical random variable	*Bootstrapping the latent space…*
N	Normal Distribution	*Bootstrapping the latent space…*
μ	Mean	*Bootstrapping the latent space…*
σ	Standard deviation	*Bootstrapping the latent space…*
T_B	Bootstrapped TumorSPACE tree	*Bootstrapping the latent space…*
b	Node TBE support	*Bootstrapping the latent space…*
k	Node spatial dispersion	*Calculating physical spatial dispersion…*
K	Ripley's reduced second moment function with border correction	*Calculating physical spatial dispersion…*

g_s	The set of spots in node g	*Calculating physical spatial dispersion…*
len_x	The x-axis range of values for a set of spots	*Calculating physical spatial dispersion…*
len_y	The y-axis range of values for a set of spots	*Calculating physical spatial dispersion…*
λ	Ripley intensity normalization factor	*Calculating physical spatial dispersion…*
r_{max}	Ripley maximum spot distance	*Calculating physical spatial dispersion…*
R	The set of spot distances used to compute spatial dispersion	*Calculating physical spatial dispersion…*
r	A particular spot distance for computing spatial dispersion	*Calculating physical spatial dispersion…*
δ	Spot pairwise physical distance	*Calculating physical spatial dispersion…*
Δ	Matrix of pairwise spot-spot physical distances	*Calculating physical spatial dispersion…*
X_{spot}	X axis physical location of a spot	*Calculating physical spatial dispersion…*
Y_{spot}	Y axis physical location of a spot	*Calculating physical spatial dispersion…*
κ	The number of spot KNN matches	*Calculating physical spatial dispersion…*
P	The set of p being tested	*Calculating physical spatial dispersion…*
n_p	The length of set P	*Calculating physical spatial dispersion…*
$Uniform([a,b])$	The Uniform Distribution between a and b	*Calculating physical spatial dispersion…*
H	The set of hyperparameters for $b, k,$ and κ	*Calculating physical spatial dispersion…*
n_H	The length of set H	*Calculating physical spatial dispersion…*
h_i	A given choice of hyperparameter values for $b, k,$ and κ	*Calculating physical spatial dispersion…*
G_{filt}	The set of internal nodes in G that meet a given set of hyperparameter bounds on b and k	*Calculating physical spatial dispersion…*
G_{filt}'	The set of G_{filt} plus the parent nodes of G_{filt} within T	*Calculating physical spatial dispersion…*
T_{filt}	Tree T filtered for internal nodes within G_{filt}'	*Calculating physical spatial dispersion…*
d	Spot pairwise spectral distance	*Prediction accuracy calculation*
I	The set of all spots in a biopsy	*Prediction accuracy calculation*
$NN_{i,\kappa}$	The set of κ nearest neighbors to spot i in latent space T	*Prediction accuracy calculation*
$spot_{i,z}$	A given nearest neighbor spot within $NN_{i,\kappa}$	*Prediction accuracy calculation*
ρ	Pearson Correlation Coefficient	*Prediction accuracy calculation*

$corr$	Pearson Correlation function	*Prediction accuracy calculation*
vec	Matrix vectorization function	*Prediction accuracy calculation*
S_{spot}	The tuple of spot locations (X_{spot}, Y_{spot})	*Prediction accuracy calculation*
T_{filt}^{opt}	The optimized TumorSPACE model for a given tumor biopsy	*Prediction accuracy calculation*
$A_{g_i}^{path}$	The full ancestral node path for an internal node g_i in any tree T	*Spatial Group (SG) depth*
$a_{g_i}^k$	The kth ancestor of an internal node g_i in any tree T	*Spatial Group (SG) depth*
σ_{node_g}	The spatial domain size of an internal node g_i in any tree T	*Spatial Group (SG) depth*
λ_{node_g}	The SG depth of an internal node g_i in any tree T	*Spatial Group (SG) depth*
G_{DA}	The subset of internal nodes within tree T that will be used for differential abundance computation	*SG-based differential abundance*
$W(a,b)$	Wilcoxon rank-sum test between a and b	*SG-based differential abundance*
$p_{g_{DA},f}$	Differential Abundance Probability at node g_{DA} for process f	*SG-based differential abundance*
$q_{g_{DA},f}$	Differential Abundance Probability at node g_{DA} for process f, empirically bootstrapped and multiple hypothesis adjusted	*SG-based differential abundance*
DA	The set of differentially abundant spots for process i at node j in a given tumor biopsy	*SG-based differential abundance*
$OR_{i,j}$	The odds ratio of independence between process i in an NSG and process j in a parent SG	*Contextual dependence of processes…*
$SLAB$	The SLAB Score for process i in a given tumor biopsy	*SG-based spatial lability (SLAB) score*
L^k	The matrix of SLAB scores composed of samples (rows) in groups K and nK	*Differential SLAB score analysis*
$MW(a,b)$	Mann-Whitney U Test between a and b	*Differential SLAB score analysis*
$p_{K,f}$	p-value of the MW test between samples in groups K vs nK for process f	*Differential SLAB score analysis*
$p_{K,f}^{shuffled}$	p-value of the MW test between samples shuffled between groups K vs nK for process f	*Differential SLAB score analysis*

714
715 *Overview*
716 Building a TumorSPACE model requires spatial transcriptomic data and two inputs from
717 SpaceRanger: (1) the raw gene UMI count matrix and (2) the spot spatial coordinate matrix.
718 Model building subsequently operates on the gene count matrix to build many models that vary
719 in hyperparameter choice. The spot spatial coordinates are then used for selecting the optimal
720 hyperparameter set that maximizes accurate recovery of spatial spot organization.
721

722 Four hyperparameters are tuned during this process: (1) the number of principal components
723 (PCs) of data-variance used for creating a latent space of the transcriptional data, (2) the limit of
724 statistical robustness for spot-spot relatedness in the latent space, (3) the spatial dispersion of
725 the nodes in the latent space hierarchical tree model, and (4) the number of KNN matches used
726 for spot spatial prediction. The following sections will first establish the model latent space and
727 compute statistical robustness and spatial dispersion properties of that latent space.
728 Subsequently, all hyperparameters will be tuned to define the optimal model for mapping
729 transcriptional content from TME spots to TME spatial organization.
730
731 _Creating a latent space_
732 The first step in building a TumorSPACE model is to create a latent space representation of the
733 gene count data that incorporates statistical bootstrapping. TumorSPACE first embeds ST-seq
734 spots into a latent space by applying singular value decomposition (SVD) to the gene count
735 matrix[62]:
736
737 $$M = U\Sigma V^T \tag{1}$$
738
739 M is the SpaceRanger gene count matrix (m spots as rows, n genes as columns), U is the left
740 singular matrix, Σ is the singular value matrix, and V is the right singular matrix. U is defined by
741 cell spots (rows) and left singular vectors (columns), where each entry is the projection of a cell
742 spot onto a left singular vector. Σ is a diagonal matrix where entries are singular values. V^T is
743 defined by genes (rows) and right singular vectors (columns) where each entry is the projection
744 of a gene onto a right singular vector.
745   First, from (1), a metric termed 'spectral distance' (D) between all spots is calculated.
746 This metric was previously developed by our laboratory in the context of analyzing phylogenetic
747 bacterial proteome content[9]. As implemented for spatial data in this manuscript, performing SVD
748 on the gene count matrix determines the extent to which each cell spot projects onto each left
749 singular vector. Therefore, a distance considering the transcriptomes of two spots can be
750 computed by measuring the difference in the projections of two spots onto a left singular vector.
751 Note, this definition of distance does not consider any information about spatial spot distribution.
752   Next, groups of left singular vectors are combined to create 'spectral groups'. These
753 groups are defined based on the eigenvalues associated with each left singular vector: left
754 singular vectors with similar eigenvalues are grouped together:
755
756 $$SG = \{sg_1, sg_2, ...\} \tag{2}$$
757
758 where SG is the total set of spectral groups, sg_1 is first set of columns extracted from U, sg_2 is
759 the second set of columns extracted from U, and so on. The concept of spectral groups was
760 also previously developed by our laboratory[38]. Defining sg_i and sg_{i+1} is done by identifying
761 larger than expected decreases in singular values between consecutive left singular vectors. To
762 compute spectral groups, a vector of differences between consecutive singular values is
763 computed for all left singular vectors. We use the upper and lower quartiles of this distribution in
764 combination with a scaling parameter alpha to define the 'expected difference' bounds between
765 singular values. Any difference in singular values outside of these bounds deviates from
766 expectation and therefore defines a spectral group (see associated GitHub code for
767 specification of parameters). The spectral distance for a pair of spots within a spectral group is
768 then computed as the Euclidean distance between spot projections onto left singular vectors
769 comprising the spectral group weighted by the eigenvalue associated with each left singular
770 vector. The summation of these distances across all spectral groups is the spectral distance,
771 $d_{i,j}$, between spots i and j.

772   After computing $d_{i,j}$ for all spots, the resulting construct is a spectral distance matrix D
773   comprised of m rows and m columns where m is the number of spots in the original gene count
774   matrix and each entry in D is the spectral distance between two spots. D is then used as input
775   for hierarchical clustering with complete linkage to result in a tree T that relates all spots in a
776   tumor sample to each other. T has m leaves and (m-1) internal vertices (nodes). The leaves are
777   the ST-seq spots and the nodes $g \in G$ represent G hierarchically ordered groupings of these
778   spots. The resulting network is the TumorSPACE latent space of the original gene count matrix.
779   The number of spectral groups is dependent on how many of the total left singular
780   vectors are considered. An increasing number of left singular vectors being included
781   corresponds directly to the inclusion of deeper principal components when computing the latent
782   space. For TumorSPACE models, the depth of principal components, 'p', is a hyperparameter
783   that is tuned for embedding the gene count matrix into a latent space.
784
785   *Bootstrapping the latent space to evaluate statistical robustness*
786   TumorSPACE does not assume that each node g arises from biological signal. Instead,
787   TumorSPACE bootstraps T using the Booster package's implementation of transfer bootstrap
788   expectation (TBE), the probability that node g appears in an empirically bootstrapped tree
789   (default settings used for Booster)[63]. For generating empirically bootstrapped trees, we applied
790   Gaussian multiplicative noise injection to the initial gene count matrix M to create a
791   "bootstrapped" gene count matrix M_B.
792
793
$$M_B = M \odot X \tag{3}$$

794
795   such that $\odot$ indicates element-wise multiplication by a normally distributed random variable
796    $X \sim N(\mu, \sigma^2)$ with $\mu = 1$ and $\sigma = 0.2$. This matrix was then used as an input to (1) and a tree was
797   created following the steps outlined in '*Creating a latent space*' to generate a bootstrapped tree
798   T_B. Bootstrapping was done 10 times for a given dataset, followed by input of the original tree T
799   and the bootstrapped trees T_B into Booster for TBE computation. This results in a labeling of the
800   original tree T's set of nodes G with TBE support values b_G such that $b_G \in [0,1]$.
801
802   *Calculating physical spatial dispersion in latent space*
803   The final property of T that is computed is the spatial dispersion k for each node comprising T.
804   Spatial dispersion is estimated for each node using Ripley's reduced second moment function
805    $K(r)$ with border correction[64,65]. Let g_s be the set of ST-seq spots within node g in T. The window
806   of physical tumor space is defined by the spot spatial coordinate matrix such that len_x indicates
807   the x-axis window length and len_y indicates the y-axis window length. We then compute λ, a
808   normalization factor for spot intensity within a spatial region, and r_{max}, a factor that incorporates
809   lambda to determine the maximum spatial distance being assessed.
810
811
$$\lambda = \frac{|g_s|}{len_x * len_y} \tag{4}$$

812
$$r_{max} = \min \{\min\{len_x, len_y\}, \sqrt{\frac{1000}{\pi * \lambda}}\} \tag{5}$$

813   where *min* denotes the minimum between a set of values. Let R be the set of spot spatial
814   distances that will be assessed, such that
815
816
$$r \in R \mid R = \{0, \frac{r_{max}}{512}, \frac{2 * r_{max}}{512}, ..., r_{max}\} \tag{6}$$

817
818   We define the physical distance δ between any two spots as
819

820
$$\delta(spot_i, spot_j) = \Delta_{i,j} = \Delta_{j,i} = \sqrt{(X_{spot_i} - X_{spot_j})^2 + (Y_{spot_i} - Y_{spot_j})^2} \qquad (7)$$

821
822 where (X_{spot}, Y_{spot}) denote the physical space coordinates for a given spot. Spatial dispersion $K(r)$
823 with border correction is then computed for all spots $g_{s,i}, \in g_s$ as

824
825
$$t^r_{g_{s,i}} = f(g_{s,i}, r) = \sum_{j=1}^{m} \mathbf{1}\{0 < \delta(g_{s,i}, spot_j) < r\} \qquad (8)$$

826

827
$$K(r) = \frac{\sum_{i=1}^{card(G)}(\mathbf{1}\{b_i \geq r\} * t^r_{g_{s,i}})}{\lambda * \sum_{i=1}^{card(G)} \mathbf{1}\{b_i \geq r\}} - \pi r^2 \qquad (9)$$

828
829 where $t(g_{s,i}, r)$ is the number of spots within distance r of a given $g_{s,i}$ and b_i is the distance from
830 spot $g_{s,i}$ to the window boundary. The general notation *card(S)* indicates the number of
831 elements in a set S, and the general notation *1{f(x)}* signifies a value of 1 when f(x) is true and a
832 value of 0 when *f(x)* is false. Finally, spatial dispersion *k* is computed by summing the absolute
833 value of *K(r)* over $r \in R$ as follows.

834
835
$$k = \sum_{r \in R} abs(K(r)) \qquad (10)$$

836
837 This calculation labels all nodes *G* in tree *T* with spatial dispersion values k_G such that
838 $k_G \in_{\mathbb{R}} [0, \infty]$.

839
840 *Hyperparameter optimization to create a TumorSPACE map*
841 TumorSPACE model optimization involves selecting the values of four hyperparameters that
842 maximize model prediction accuracy (described in '*Prediction Accuracy Calculation*') for a given
843 dataset. These hyperparameters tune three properties of tree *T* – principal component depth *p*
844 (from '*Creating a latent space*'), node TBE support *b* (from '*Bootstrapping the latent space to*
845 *evaluate statistical robustness*'), node spatial dispersion *k* (from '*Calculating physical spatial*
846 *dispersion in latent space*') – as well as one property of accuracy computation, the number of
847 spot KNN matches κ. We perform hyperparameter tuning as a nested grid search by tuning *p* as
848 an outer layer and then optimizing $[b, k, \kappa]$ for a given value of *p*.
849   First, a set of PC depth values (n_p where default is set to 10) is randomly selected to
850 create a set $P = \{p_1, p_2, \dots, p_{n_p}\}$. The PCs termed p_i are chosen on a logarithmic interval
851 between a minimum and maximum PC depth, which is the rank of the gene count matrix *M*.
852 Next, a matrix of three hyperparameter values, $H = \{h^{(1)}_{1 \dots n_H}, h^{(2)}_{1 \dots n_H}, h^{(3)}_{1 \dots n_H}\}$, are created where the
853 vectors $h^{(1)}$, $h^{(2)}$, and $h^{(3)}$ are independently sampled from distributions as follows.

854
855
$$h^{(1)} \in_{\mathbb{R}} 10^{X*log10\left(\frac{b_{max}+1}{b_{min}+1}\right)+log10(b_{min}+1)} - 1 \qquad (11)$$

856
$$h^{(2)} \in_{\mathbb{R}} 10^{X*log10\left(\frac{k_{max}+1}{k_{min}+1}\right)+log10(k_{min}+1)} \qquad (12)$$

857
$$h^{(3)} \in_{\mathbb{Z}} round(10^{X*log10\left(\frac{\kappa_{max}+1}{\kappa_{min}+1}\right)+log10(\kappa_{min}+1)}) \qquad (13)$$

858
859
860 In (*11-13*), X is a random variable drawn from $Uniform([0,1])$. Default values for
861 hyperparameter bounds are $b_{min} = 0$, $b_{max} = 0.5$, $k_{min} = 0$, $k_{max} = 1$ $\kappa_{min} = 5$, $\kappa_{max} = 300$. A
862 minimum of $n_H = 100$ sets of $\{h^{(1)}, h^{(2)}, h^{(3)}\}$ are initially sampled, after which additional sets are
863 sampled until prediction accuracy optimization has converged. Prediction accuracy convergence

864 is reached when the difference in prediction accuracy (defined below in '*Prediction Accuracy*
865 *Calculation*') for the top 2 scoring hyperparameter sets is less than 0.05. For a given
866 hyperparameter set h_i, the TumorSPACE tree T is filtered for the set of nodes G_{filt} such that
867 each node in G_{filt} satisfies
868

869 $$b \geq h_i^{(1)} \quad \text{AND} \quad k \geq h_i^{(2)} \tag{14}$$
870

871 The final filtered tree, T_{filt}, comprises the set of nodes G_{filt}', which consists of G_{filt} as well as the
872 complete set of parent nodes from which G_{filt} descend even if those parent nodes do not meet
873 the criteria in *(14)*, along with all ST-seq spots.
874

875 *Prediction accuracy calculation*
876 To identify the TumorSPACE model properties that were optimized for predicting spot spatial
877 locations from transcriptomic data, we masked the physical location of each ST-seq spot and
878 identified its k nearest neighbors in the TumorSPACE latent space by minimizing spectral
879 distance.
880

881 For any masked spot i amongst all spots I, we can define its κ nearest neighbors $NN_{i,\kappa}$ as
882

883 $$NN_{i,\kappa} = argmin_{j \in J}^{\kappa} \left(d(spot_i, spot_j) \right) \tag{15}$$
884

885 where $i \in I$, $\kappa \in h^{(3)}$ as defined in *(13)*, J is the set of all spots other than spot i, and $argmin^{\kappa}$
886 selects the set of κ spots with the smallest spectral distance relative to spot i. To prevent
887 overfitting, we identified for each $spot_{i,z} \in NN_{i,\kappa}$ a randomly chosen $spot'_{i,z}$ that belongs to the
888 internal node $g^{i,z}$ within T_{filt} immediately ancestral to $spot_{i,z}$.
889

890 We then estimated the location of masked *spot i* based on the x and y locations of the
891 corresponding $spot'_{i,z}$ spots.
892

893 $$\hat{X}_{spot_i} = \frac{1}{\kappa}\sum_{z=1}^{\kappa} X_{spot'_{i,z}} \text{ and } \hat{Y}_{spot_i} = \frac{1}{\kappa}\sum_{z=1}^{\kappa} Y_{spot'_{i,z}} \tag{16}$$
894

895 Finally, we computed the Pearson Correlation ρ between the vectorized matrix Δ_{actual} of
896 pairwise actual spot-spot physical distances and the vectorized matrix $\Delta_{predicted}$ of pairwise
897 predicted spot-spot physical distances.
898

899 $$\Delta_{actual}[i,j] = \sqrt{(X_{spot_i} - X_{spot_j})^2 + (Y_{spot_i} - Y_{spot_j})^2} \tag{17}$$

900 $$\Delta_{predicted}[i,j] = \sqrt{(\hat{X}_{spot_i} - \hat{X}_{spot_j})^2 + (\hat{Y}_{spot_i} - \hat{Y}_{spot_j})^2} \tag{18}$$

901 $$\rho = corr\left(vec(\Delta_{actual}), vec(\Delta_{predicted})\right) \tag{19}$$
902

903 where *vec()* indicates matrix vectorization to a single column and *corr()* indicates Pearson
904 Correlation. To compute a null distribution for ρ using empirical bootstrapping of actual versus
905 predicted spot locations in a given dataset, we shuffled the vector $\hat{S}_{spot_i} = (\hat{X}_{spot_i}, \hat{Y}_{spot_i})$ without
906 replacement and then re-computed *(17-18)* using this shuffled vector $\hat{S}_{spot_i}^{shuffled}$ of predicted spot
907 locations.
908

909
$$\hat{S}_{spot}^{shuffled} = \{K \subseteq \hat{S}_{spot_i} | \; card(K) = card(I)\} = (\hat{X}_{spot}^{shuffled}, \hat{Y}_{spot}^{shuffled}) \qquad (20)$$

910
$$\Delta_{predicted}^{shuffled}[i,j] = \sqrt{(\hat{X}_{spot_i}^{shuffled} - \hat{X}_{spot_j}^{shuffled})^2 + (\hat{Y}_{spot_i}^{shuffled} - \hat{Y}_{spot_j}^{shuffled})^2} \qquad (21)$$

911
$$\rho^{shuffled} = corr\left(vec(\Delta_{actual}), vec(\Delta_{predicted}^{shuffled})\right) \qquad (22)$$

912

913 For **Fig. 1B**, $\rho^{shuffled}$ is computed for 100 shuffles and the maximum ρ is taken as the 'null'
914 prediction value. The null distribution is plotted in the grey distribution in **Fig. 1B**.
915

916 Finally, the optimal TumorSPACE model T_{filt}^{opt} is found that maximizes ρ across hyperparameter
917 sets P and H.
918

919
$$T_{filt}^{opt} = argmax_{p \in P, h \in H}^1 (\rho_{p,h}) \qquad (23)$$

920
921

922 *TumorSPACE model outputs*
923 For a given input tumor ST-seq dataset, the output from TumorSPACE includes: (1) the
924 TumorSPACE model T_{filt}^{opt}, (2) the Pearson Correlation estimate ρ, and (3) the set of predicted
925 spot locations $(\hat{X}_{spot_i}, \hat{Y}_{spot_i})$ for all ST-seq spots. The final set of internal nodes within T_{filt}^{opt} are
926 termed Spatial Groups (SGs).
927

928 *Spatial Group (SG) depth*
929 We computed SG depth as a measurable quantity that describes how a given SG relates to the
930 other parts within a TumorSPACE model. As such, we first define 'SG depth' as a property of all
931 SGs within a TumorSPACE model, and next define 'spot SG depth' as a property of all spots
932 within the gene count matrix.
933

934 To first define SG depth, we compute the complete ancestral node path for any internal node g_i
935 within T_{filt}^{opt} as
936

937
$$A_{g_i}^{path} = \{a_{g_i}^0, a_{g_i}^1, a_{g_i}^2, ..., a_{g_i}^n\} \qquad (24)$$

938
939 such that
940
$$a_{g_i}^0 = g_i \qquad (24)$$

941
942
$$a_{g_i}^{k+1} = A(a_{g_i}^k) \; for \; k \in [1, n-1] \qquad (25)$$

943
944
$$a_{g_i}^n \in G \qquad (26)$$

945

946 $a_{g_i}^k$ indicates the kth ancestral node of node g_i, $A(node)$ denotes the immediate ancestral node of
947 a given node in T_{filt}^{opt}, and G is the set of internal nodes in T_{filt}^{opt}. By definition, $a_{g_i}^n$ will be the root
948 node of T_{filt}^{opt}. We next define the spatial domain size σ_{node_g} for a given node g as the mean
949 spot-spot physical distance between all spots within g.
950

951
$$\sigma_{node_g} = \frac{\sum_{i=1}^I \sum_{j=1}^J \delta(spot_i, spot_j)}{I * J} \; where \; I = J = card(g_s) \qquad (27)$$

952

953 Finally, we identify the subset of nodes $A_{g_i}^{nested}$ within $A_{g_i}^{path}$ that satisfy the condition whereby
954 the $(k+1)^{th}$ node is equal to or larger in spatial domain size than the kth node in that path.
955

$$A_{g_i}^{nested} \in A_{g_i}^{path} \mid \begin{cases} A_{g_i}^{path} = \{a_{g_i}^0, a_{g_i}^1, a_{g_i}^2, ..., a_{g_i}^n\} \\ A_{g_i}^{nested} = \{a_{g_i}^0, a_{g_i}^1, a_{g_i}^2, ..., a_{g_i}^k\} \\ \sigma_{a_{g_i}^{l+1}} \geq \sigma_{a_{g_i}^l} \end{cases} \quad (28)$$

957
958 where $k \leq n$ and $0 \leq l \leq k$. The SG depth, λ_{node_g}, for a given internal node g_i is defined to be
959 the number of ancestral generations that satisfy this condition of spatial domain nesting.
960

$$\lambda_{node_g} = card(A_{g_i}^{nested}) - 1 \quad (29)$$

962
963 *SG-based differential abundance*
964 Differential abundance calculation requires two inputs: (1) an optimized TumorSPACE model
965 T_{filt}^{opt} and (2) a spot-by-feature matrix *F*. We computed differential abundance using three types
966 of biological processes: genes, pathways, and deconvoluted cell type proportions. Computation
967 of gene count, pathway usage, and cell type proportion matrices are described in the
968 *'SpaceRanger'*, *'GSVA'*, and *'SpaCET'* Methods sections, respectively. The gene count matrix is
969 normalized by the spot-wise total UMI count.
970
971 First, we identified a subset of SGs $G_{DA} \in G$ at which DA will be computed. We set a minimum of
972 10 spots that must be present in both a given SG $g_{DA} \in G_{DA}$ and in its sibling node g'_{DA} (e.g. *A*
973 and *A'* in **Fig. 2A**) for inclusion within G_{DA}.
974

$$G_{DA} = [g_{DA} \in G'_{filt} \mid card(C(g_{DA})) \geq 10 \, \& \, card(C(g'_{DA})) \geq 10] \quad (30)$$

976
977 where *C(n)* indicates the row indices within matrix *F* of the spots descending from SG g_{DA}.
978 Subsequently, for each node g_{DA} and process *f*, the spot-wise process values between g_{DA} and
979 g'_{DA} are compared using a two-sided Wilcoxon Rank Sum Test, where the test p-value is given
980 by *W(a,b)*.
981

$$p_{g_{DA},f} = W(F_{C(g_{DA}),f}, F_{C(g'_{DA}),f}) \quad (31)$$

983
984 To facilitate empirical correction for multiple hypothesis testing, we perform 20 shuffles of the
985 process values between g_{DA} and g'_{DA}, followed by computation of the Wilcoxon p-value between
986 these shuffles. Let $C_{n_{total}}$ be the concatenation of spot indices $C(g_{DA})$ and $C(g'_{DA})$.
987

$$C_{g_{total}} = C(g_{DA}) + C(g'_{DA}) \quad (32)$$

989

$$C_{g_{total}}^{shuffled} = \{K \subseteq C_{g_{total}} \mid card(K) = card(C_{g_{total}})\} = C_{g_{DA}}^{shuffled} + C_{g'_{DA}}^{shuffled} \quad (33)$$

991

$$C_{g_{DA}}^{shuffled} = C_{g_{total}}^{shuffled}[1:card(C(g_{DA}))] \quad (34)$$

993

$$C_{g'_{DA}}^{shuffled} = C_{g_{total}}^{shuffled}[(card(C(g_{DA})) + 1):(card(C(g_{DA})) + card(C(g'_{DA})))] \quad (35)$$

995

996
$$p_{g_{DA},f}^{shuffled} = W\left(F_{C_{g_{DA}}^{shuffled},f}, F_{C_{g'_{DA}}^{shuffled},f}\right) \tag{36}$$

997

998 Let $P_{g_{DA},j}^{shuffled} = \{p_{g_{DA},j,1}^{shuffled}, p_{g_{DA},j,2}^{shuffled}, \dots, p_{g_{DA},j,n}^{shuffled}\}$ be the set of n DA probabilities for node g_{DA}
999 and shuffle j, where n is the number of processes in F. Then, a given process is found to be
1000 differentially abundant at a given node if its unadjusted p-value, $p_{g_{DA},f}$, is less than the minimum
1001 of all shuffled probabilities for that node. To assign the direction of process abundance change
1002 for nodes with significant abundance changes, given that our test examines relative changes in
1003 expression between g_{DA} and in its sibling node g'_{DA}, we defined the larger of the two nodes as
1004 having a "baseline expression profile" for that shared local transcriptional and spatial context.
1005 Conversely, the smaller of the two nodes was defined as having either increased or decreased
1006 abundance relative to the larger node.
1007

1008 _Contextual dependence of processes based on architecture of SGs_
1009 To determine whether differentially abundant processes within NSGs were impacted by the
1010 differentially abundant processes of their parent SGs, we computed the odds ratio test for
1011 independence as follows. Let $f_i \in F$ and $f_j \in F$ denote two biological processes drawn from the
1012 set of all pathways and cell types identified (see _'GSVA'_ and _'SpaCET'_ sections). Across all
1013 TumorSPACE models, we identified the set of NSG-parent SG pairs – denoted by (N_i, P_j) –
1014 such that N_i^+ and N_i^- indicate the subset of NSGs where process i was increased or decreased
1015 in abundance, respectively, and P_i^+ and P_i^- indicate the subset of parent SGs where
1016 process j was increased or decreased in abundance, respectively. Then, the odds ratio of
1017 independence $OR_{i,j}$ was defined as,
1018

1019
$$OR_{i,j} = \frac{\left(card(N_i^+, P_i^+)\big/card(N_i^-, P_i^+)\right)}{\left(card(N_i^+, P_i^-)\big/card(N_i^-, P_i^-)\right)} \tag{37}$$

1020

1021 Standard definitions were used for calculation of odds ratio standard error and p-values[66].
1022

1023 _SG-based spatial lability (SLAB) score_
1024 Given a single TumorSPACE model T_{filt}^{opt} and a process f_i for which differential abundance has
1025 been computed in T_{filt}^{opt}, we define the SLAB score as follows. Let G^{f_i} be the set of SGs in T_{filt}^{opt}
1026 in which the process f_i is differentially abundant ($q < 0.05$). For each node $g_k^{f_i} \in G^{f_i}$, this
1027 means that process f_i is differentially abundant between $g_k^{f_i}$ and its sister node $g_k^{f_i\prime}$ in T_{filt}^{opt}.
1028 First, we identify which of the nodes, either $g_k^{f_i}$ or $g_k^{f_i\prime}$, contains the fewer number of spots. This
1029 node is defined as the node with either increased or decreased abundance of process f_i, while
1030 the node with the greater number of spots is considered to be the 'baseline' abundance state for
1031 process f_i in that subset of the tumor biopsy. $DA\left(T_{filt}^{opt}, f_i, g_k^{f_i}\right)$ describes the set of spots with
1032 differential abundance in process f_i for TumorSPACE model T_{filt}^{opt} at node $g_k^{f_i}$:
1033

1034
$$DA\left(T_{filt}^{opt}, f_i, g_k^{f_i}\right) = \{\min\left(\left[C\left(g_k^{f_i}\right), C\left(g_k^{f_i\prime}\right)\right]\right) \mid g_k^{f_i} \in G^{f_i}\} \tag{38}$$

1035

1036 Next, we compute the union of those differentially abundant spots and compute the fraction that
1037 these spots constitute compared to the total set of spots _I_ in the biopsy as a whole.
1038

1039

$$SLAB\left(T_{filt}^{opt}, f_i\right) = \frac{card(U\{DA\left(T_{filt}^{opt}, f_i, g_k^{f_i}\right) \mid g_k^{f_i} \in G^{f_i}\})}{card(I)} \qquad (39)$$

1041

1042   For **Fig. 3D,E**, SLAB scores were computed using either only NSGs or only non-NSGs as the
1043   input set of SGs used for computing G^{f_i}.

1044

1045   *SLAB score correlation with bulk expression*
1046   For correlation of genome-wide SLAB scores with bulk gene expression, as in **Fig. 2B** and
1047   **Extended Data Fig. 3**, we did the following. First, we identified the set of all dataset-gene pairs
1048   for which the gene had greater than 0 UMIs detected per spot and a non-zero SLAB score in
1049   that dataset. Next, to enable computing correlation statistics, we identified genes with greater
1050   than 10 dataset entries in the filtered dataset-gene pair list. For these genes, we computed the
1051   Pearson Correlation estimate and p-value between SLAB score and mean spot UMI count
1052   across datasets. Correction for multiple hypothesis testing was done using the Benjamini-
1053   Hochberg method with a corrected q-value threshold of 0.05[67].

1054

1055   *Spatial lability pan-tumor classification*
1056   Given the set of SLAB scores that were computed for all available genes for each of the 96
1057   datasets within the pan-tumor ST-seq database (see 'ST-seq dataset download and alignment'),
1058   we aligned these score vectors into a matrix M_{SLAB}^{Pan} such that each dataset was a row and each
1059   gene was a column. For any instances where a gene had mapped reads in one dataset but not
1060   another – thus resulting in blank cells in this matrix – the score within this matrix was set to zero.
1061   Next, Euclidean distance was computed between each pair of rows, resulting in a distance
1062   matrix of dimensions 96 x 96 that compared all datasets to each other. Finally, the Unweighted
1063   Pair Group Method with Arithmetic mean (UPGMA) algorithm was used for constructing a
1064   hierarchical tree relating datasets to each other (**Extended Data Fig. 12**)[68].

1065

1066   For defining tumor groups from this tree, we used the path of tree connections containing the
1067   highest number of tumors as our reference point. From this 'main path', we labeled any
1068   diverging branchpoints with labels A, B, C, … as shown in **Fig. 3B**. Whenever a group was
1069   defined (e.g. group 'A'), the remaining 'main path' tumors were defined as *not* in that group (e.g.
1070   group 'nA', where 'n' indicates 'not').

1071

1072   *Building across-tumor spatial models*
1073   To evaluate the ability of spatial organization in one tumor biopsy (training) to predict spatial
1074   organization in another tumor biopsy (testing), we applied the TumorSPACE workflow in the
1075   following manner. First, an alignment was performed between the training tumor gene count
1076   matrix and the testing tumor gene count matrix since the experiments may have used distinct
1077   probe sets and thus mapped reads to non-identical sets of genes. Next, the testing tumor spot
1078   transcriptomes were projected into the latent space of the training data, after which spectral
1079   distances were computed to determine similarity between training tumor spots and testing tumor
1080   spots. Finally, the training tissue TumorSPACE model *T* was optimized on the same properties
1081   as before (see '*Hyperparameter optimization to create a TumorSPACE map*') by tuning spatial
1082   predictions on the training tissue and then evaluating prediction quality on the testing tissue.

1083

1084   For latent space projection between the aligned gene count matrices, we denote the aligned
1085   gene count matrices for training and testing tissues as M_{tr} *(m_1 x g)* and M_{te} *(m_2 x g)* respectively.
1086   As follows from (1), we computed SVD on M_{tr} as
1087

$$M_{tr} = U_{tr} * \Sigma_{tr} * V_{tr}^T \tag{40}$$

We then projected M_{te} into the latent space U_{tr} as follows. The value of the hyperparameter p is the value of p that maximizes spatial prediction in the training tumor dataset.

$$U_{te} = M_{te} * (V_{tr}^{T\,(1:p)})^{-1} * (\Sigma_{tr}^{(1:p)})^{-1} \tag{41}$$

where $(V_{tr}^{T\,(1:p)})^{-1}$ is computed using the pseudo-inverse. Vertical concatenation of U_{tr} and U_{te} yields a joint U matrix $U_{tr,te}$. From $U_{tr,te}$ and Σ_{tr}, we compute spectral distance between all spots in M_{tr} and M_{te} as $D_{tr,te}$.

$$D_{tr,te} = spectraldistances(U_{tr,te}^{(1:p)}, \Sigma_{tr}^{(1:p)}, getintervals\left(U_{tr,te}^{(1:p)}\right)) \tag{42}$$

Finally, we filtered matrix $D_{tr,te}$ for the matrix of spectral distances $D'_{tr,te}$ of shape m_2 x m_1 that contains pairwise distances of spots only between M_{tr} and M_{te}. This operation removes intra-group spectral distance comparisons for both M_{tr} and M_{te} and keeps only inter-group spectral distance comparisons between pairs of spots in M_{tr} and M_{te}.

$$D'_{tr,te} = D_{tr,te}^{((m_1+1):(m_1+m_2),1:m_1)} \tag{43}$$

Differential SLAB score analysis
Using the tumor groups as defined in '*Spatial lability pan-tumor classification*', we compared each group K to the set nK of 'main path' tumors divergent from that group.

To compare gene-level SLAB scores, we first compose the matrix L^k of SLAB scores where L^k has $k + k_n$ rows corresponding to tumors $k \in K$ and $k_n \in nK$ and F columns where $f \in F$ constitutes the full set of genes. Next, for each gene f, we compare the tumors in K and nK where $C(X)$ indicates the row indices within matrix L^k that correspond to tumors in either group. Comparison is performed using a Mann-Whitney U Test, where the test p-value is given by $MW(a,b)$.

$$p_{K,f} = MW(L_{C(K),f}^k, L_{C(nK),f}^k) \tag{44}$$

To facilitate empirical correction for multiple hypothesis testing, we perform 1000 shuffles of the SLAB counts between K and nK, followed by computation of the MW p-value between these shuffles. Let $C_{K_{total}}$ be the concatenation of row indices $C(K)$ and $C(nK)$.

$$C_{K_{total}} = C(K) + C(nK) \tag{45}$$

$$C_{K_{total}}^{shuffled} = \{J \subseteq C_{K_{total}} | card(J) = card(C_{K_{total}})\} = C_K^{shuffled} + C_{nK}^{shuffled} \tag{46}$$

$$C_K^{shuffled} = C_{K_{total}}^{shuffled}[1: card(C(K))] \tag{47}$$

$$C_{nK}^{shuffled} = C_{K_{total}}^{shuffled}[(card\left(C(K)\right) + 1):(card(C(K)) + card(C(nK)))] \tag{48}$$

$$p_{K,f}^{shuffled} = MW(L_{C_K^{shuffled},f}^k, L_{C_{nK}^{shuffled},f}^k) \tag{49}$$

1134

1135   Let $P_{K,j}^{shuffled} = \{p_{K,j,1}^{shuffled}, p_{K,j,2}^{shuffled}, ..., p_{K,j,n}^{shuffled}\}$ be the set of n probabilities for group K and
1136   shuffle j, where n is the number of genes in F. Then, a given gene is found to have a differential
1137   SLAB score between a given grouping K vs nK if its unadjusted p-value, $p_{K,f}$, is less than the 5th
1138   percentile ($q = 0.05$) of all shuffled probabilities.

1139

1140   To compare pathway-level SLAB scores, we used either over-representation analysis (ORA) or
1141   gene-set enrichment analysis (GSEA). For both analyses, we computed enrichment for the set
1142   of Reactome pathways within the MSigDB database[69,70] (**Supplementary Table 5**). ORA was
1143   performed using Enrichr with default parameters, which uses a Fisher exact test to compute
1144   enrichment of a gene list for a given pathway[71]. The background gene set used was the set of
1145   all genes with mapped reads in any sample. GSEA was performed using 20,000 permutations
1146   with the "signal-to-noise" ratio used for ranking[69]. For both ORA and GSEA, correction for
1147   multiple hypothesis testing was implemented by using a false discovery rate threshold of < 0.1.

1148

1149   *Classification of NSCLC datasets by pan-tumor immune spatial lability*
1150   For comparison of out-of-sample NSCLC tumors to pan-tumor spatial lability groups shown in
1151   **Fig. 3B**, we first computed SLAB scores for all genes and aligned the score vectors to match
1152   the columns (genes) of the pan-tumor SLAB score matrix M_{SLAB}^{Pan}. Any genes with no detectable
1153   reads for a given sample had their SLAB score set to zero. We called this new matrix M_{SLAB}^{NSCLC}.
1154   For every pair of rows $(r_{p_i}^{Pan}, r_{n_j}^{NSCLC})$, where $r_{p_i}^{Pan}$ indicates the score vector for sample $p_i \in P$ in
1155   the pan-tumor database and $r_{n_j}^{NSCLC}$ indicates the score vector for sample $n_j \in N$ in the NSCLC
1156   out-of-sample dataset, we computed the Euclidean distance D_{p_i,n_j}^{SLAB} that describes the similarity
1157   between these two samples with respect to their SLAB scores. For a given NSCLC sample n_j,
1158   we identified the pan-tumor dataset p_i with the lowest Euclidean distance to n_j and assigned n_j
1159   to the same spatial lability class as p_i.

1160

1161   For defining immune spatial lability, since tumor groups 'C' and 'E' both demonstrated
1162   enrichment in SLAB score for immune biology components, we defined 'nE' tumors as immune
1163   spatially invariant (ISI) and tumors in groups A, B, C, D, or E as immune spatially labile (ISL).

1164

1165   *Classification of NSCLC datasets using bulk expression and published gene sets*
1166   To determine whether classification of tumor datasets by either (1) bulk expression versus
1167   SLAB score or (2) previously published gene sets for NSCLC IO response was predictive of
1168   PFS in our NSCLC cohort, we performed the following analysis.

1169

1170   First, we computed aligned matrices as described in '*Spatial lability pan-tumor classification'* for
1171   both the pan-tumor datasets and the NSCLC datasets where matrices contained either bulk
1172   expression data or SLAB score data. For bulk expression, we computed the mean spot-wise
1173   UMI count for any given gene. Second, we filtered the aligned matrices for subset of columns
1174   (genes) described by a particular gene set or used all columns for the 'all genes' analysis. Third,
1175   we computed a hierarchical tree using the pan-tumor data and identified the best matches to
1176   datasets within that tree for all NSCLC datasets as described in '*Spatial lability pan-tumor*
1177   *classification'.* Fourth, K-means clustering with K = 2 was applied to the Euclidean distances
1178   between all pairs of 'best match' pan-tumor datasets. K-means clustering was performed 100
1179   times for each condition using different random seeds each time. Finally, the two classes that
1180   were defined were used to classify the NSCLC cohort based on the matching performed
1181   between the NSCLC tumors and the pan-tumor datasets in the third step described above.

1182   These classes were subsequently applied to survival analysis (described below in '*Survival*
1183   *analysis'*) to determine if they were predictive of NSCLC ICB outcomes.
1184
1185   **Survival analysis**
1186   For survival analysis we used the R 'survival' package to model progression-free survival (PFS)
1187   as a function of possible confounder variables (Treatment regimen, KRAS mutation status) or
1188   classification variables (PD-L1 multi-class, PD-L1 binary, ISL/ISI, bulk expression- and SLAB
1189   score- gene sets). For confounder analysis, outcomes were modeled using Cox's univariate
1190   proportional hazards model. For Kaplan-Meier survival curves stratified by classification
1191   variables, survival was estimated using the Kaplan-Meier method and reported p-values were
1192   calculated using the log rank statistical test. For censored data labeling, 1 indicates that PFS
1193   was observed while 0 indicates the patient was censored for PFS.
1194
1195   **GSVA**
1196   Gene set variation analysis (GSVA) estimates GSVA pathway enrichment scores for a given set
1197   of pathways from gene expression data[72]. It requires (1) the spot-by-gene count matrix from
1198   SpaceRanger and (2) a list of pathway gene sets. We used a subset of the KEGG pathways
1199   from the MSigDB database[69,73] (**Supplementary Table 6**). The 'KCDF' parameter was set to
1200   "none", which enforces a direct estimation of cumulative density function without assuming a
1201   kernel function. Otherwise, default parameters were used.
1202
1203   **SpaCET**
1204   SpaCET estimates deconvoluted cell type proportions within spots of an ST-seq experiment[39]. It
1205   requires the user to supply (1) the SpaceRanger gene count matrix as input and (2) a value for
1206   the 'cancerType' parameter to define the SpaCET library scRNA-seq datasets used for cell type
1207   definition. The 'cancerType' values chosen for each ST-seq dataset are listed in
1208   **Supplementary Table 7**. Otherwise, default parameters and commands were used as per the
1209   repository instructions (https://data2intelligence.github.io/SpaCET/articles/visium_BC.html).
1210
1211   **CODEX multiplexed immunofluorescence - analysis**
1212
1213   *Cell segmentation*
1214   Following image acquisition and pre-processing (see '*Experimental method details: CODEX*
1215   *multiplexed immunofluorescence'*), we applied the neural network-based cell segmentation tool,
1216   DeepCell, on the DAPI channel for nuclei identification[74]. Next, these nuclei segmentation
1217   masks were used to estimate whole cell segmentation boundaries using the
1218   'skimage.morphology.binary_dilation' function in the Python scikit-image package[75]. This
1219   function dilates nuclear segmentation boundaries by stochastically flipping pixels into the mask
1220   boundary with a probability equal to the fraction of positive neighboring pixels for 9 cycles. We
1221   then computed mean expression for each antibody across pixels within each whole cell
1222   segmentation boundary, which we define as the signal intensity $Signal_i^t$ for cell *i and* target *t*.
1223
1224   *Cell-level quality control*
1225   Since there is technical variation in CODEX staining and imaging quality, we applied multiple
1226   quality control filters to eliminate cells with atypical quality characteristics. First, we defined for
1227   cell *i* the signal sum Σ_i, mean μ_i, standard deviation σ_i, and coefficient of variation CoV_i across
1228   the set of targets *T*, composed of DAPI + all antibodies in **Supplementary Table 8**.
1229
1230

$$\Sigma_i = \sum_t Signal_i^t \, for \, t \, \in T \qquad\qquad (50)$$

1231

$$\mu_i = \frac{\Sigma_i}{card(T)} \tag{51}$$

$$\sigma_i = \sqrt{\frac{\sum_t (Signal_i^t - \mu_i)^2}{card(T)}} \tag{52}$$

$$CoV_i = \frac{\sigma_i}{\mu_i} \tag{53}$$

We then filtered cells for analysis only when Σ_i, CoV_i, and $Signal_i^{DAPI}$ fall within the $5 - 95\%$ of values for cells within that particular sample (**Extended Data Fig. 13A**). Let I indicate the set of cells within a single sample. Then,

$$cells_{filt} \in cells_I \mid \begin{cases} quantile(\Sigma_I, 0.05) \leq \Sigma_f \leq quantile(\Sigma_I, 0.95) \\ quantile(CoV_I, 0.05) \leq CoV_f \leq quantile(CoV_I, 0.95) \\ quantile(Signal_I^D, 0.05) \leq Signal_f^D \leq quantile(S \quad gnal_I^D, 0.95) \end{cases} \tag{54}$$

where Σ_f, CoV_f, and $Signal_f^D$ denote the signal sum, signal CoV, and DAPI intensity signal for a given cell f in $cells_{filt}$. We found that excluded cells tended to be found along tissue borders (**Extended Data Fig. 13B**).

Signal normalization
We normalized signal intensities for (1) variation in local background and (2) variation in signal distribution between samples.

To correct for variation in local background, we divided each sample into 100 equally sized bins and used multi-Gaussian modeling for each target $t \in T$ to identify the upper limits of that marker's local null distribution. Let i and j represent the bin numbers in the *x* and *y* directions respectively. Then we denote *cells*$_{i,j}$ as the set of cells in a given sample bin *(i,j)* and $Signal_{i,j}^t$ as the set of signal intensities for marker *t* for *cells*$_{i,j}$. We used the 'mclust' R package to fit 2 Gaussians to $Signal_{i,j}^t$ for all values of *i*, *j*, and *t*. Then we defined the upper bound $Background_{i,j}^t$ of the null distribution as the 95% percentile of that distribution for a given bin and marker. We found wide variation in the distributions of $Background_{i,j}^t$ for different targets *t* and for different samples, underscoring the need to use target-specific background correction (**Extended Data Fig. 14A, B**). Finally, we subtracted $Background_{i,j}^t$ from $Signal_{i,j}^t$ as a correction for local background signal variation.

$$i, j \in_{\mathbb{Z}} \{1, 2, 3, \dots, 10\} \tag{55}$$

$$Signal_{i,j}^t \sim N(\mu_1, \sigma_1^2) + N(\mu_2, \sigma_2^2) \text{ where } \mu_1 < \mu_2 \tag{56}$$

$$Background_{i,j}^t = \mu_1 + 1.645 * \frac{\sigma_1}{\sqrt{card(cells_{i,j})}} \tag{57}$$

$$Norm_{i,j}^t = Signal_{i,j}^t - Background_{i,j}^t \tag{58}$$

To minimize variation in signal quantitation between samples, we then scaled the intensity distribution for each target to match across both DLBCL samples, using 'DLBCL Patient 1' as a reference for scaling. Let $Norm_i^t$ and $Scale_i^t$ indicate the distribution of normalized and scaled

1275 intensities, respectively, from (*54*) for target *t* and DLBCL patient *i*. Let *mean* and *sd* indicate the
1276 mean and standard deviations of these intensity distributions.

1277

1278 $$Scale_i^t = \frac{Norm_i^t - mean(Norm_i^t)}{sd(Norm_i^t)} * sd(Norm_1^t) + mean(Norm_1^t) \qquad (59)$$

1279

1280 *Cell type classification*
1281 Cell types were identified from CODEX data using the following thresholds on the scaled
1282 intensities $Scale_i^t$. Let *cells_all* indicate the set of all cells across both DLBCL samples. Let
1283 $cells_c \in cells_{all}$ indicate the subset of these cells classified as class *c* for all cell types $c \in C$.
1284 The limits for each cell-type defining marker in the following definitions were identified and
1285 tested iteratively to minimize the fraction of 'Unidentifiable' cells while maintaining specific
1286 classifications for each cell type (**Extended Data Fig. 14C**).

1287

1288 $$cells_{CAF} \in cells_{all} \mid \begin{cases} Scale_i^{aSMA} > 0.25 \ or \\ Scale_i^{Vimentin} > 10 \end{cases} for \ i \in cells_{CAF} \qquad (60)$$

1289

1290 $$cells_{endothelial} \in cells_{all} \mid \begin{cases} Scale_i^{CD31} > 2.5 \ or \\ Scale_i^{CD141} > 2 \end{cases} for \ i \in cells_{endothelial} \qquad (61)$$

1291

1292 $$cells_{DLBCL} \in cells_{all} \mid \begin{cases} Scale_i^{CD38} > 4 \ or \\ Scale_i^{CD20} > 10 \ or \\ Scale_i^{CD21} > 20 \ or \\ Scale_i^{CD79a} > 0.25 \end{cases} for \ i \in cells_{DLBCL} \qquad (62)$$

1293

1294 $$cells_{CD4\,T} \in cells_{all} \mid \begin{cases} \begin{cases} Scale_i^{CD3e} > 50 \ and \\ Scale_i^{CD4} > 15 \end{cases} for \ i \in cells_{CD4\,T} \end{cases} \qquad (63)$$

1295

1296 $$cells_{CD8\,T} \in cells_{all} \mid \begin{cases} \begin{cases} Scale_i^{CD3e} > 50 \ and \\ Scale_i^{CD4} < 15 \ and \\ Scale_i^{CD8} > 5 \end{cases} for \ i \in cells_{CD8\,T} \end{cases} \qquad (64)$$

1297

1298 $$cells_{cDC} \in cells_{all} \mid \begin{cases} \begin{cases} Scale_i^{CD11c} > 15 \ or \\ Scale_i^{CD141} > 2 \end{cases} for \ i \in cells_{cDC} \end{cases} \qquad (65)$$

1299

1300 $$cells_{macrophage} \in cells_{all} \mid \begin{cases} \begin{cases} Scale_i^{CD11c} < 15 \ and \\ Scale_i^{CD68} > 50 \end{cases} for \ i \in cells_{macrophage} \end{cases} \qquad (66)$$

1301
1302

1303 $$cells_{neutrophil} \in cells_{all} \mid \begin{cases} \begin{cases} Scale_i^{MPO} > 5 \ or \\ Scale_i^{CD66} > 0.25 \end{cases} for \ i \in cells_{neutrophil} \end{cases} \qquad (67)$$

1304

1305 For cells that were classified into multiple classes by these criteria, we labeled cells as "DLBCL"
1306 if one of their multiple class labels was "DLBCL" and otherwise labeled them as "Unidentifiable".
1307

As an orthogonal validation of SpaCET-based cell type deconvolution, we observed high concordance (R = 0.99) in cell type classification between transcriptional inference and IF-based classification (**Extended Data Fig. 15, Supplementary Table 9**).

CoV analysis of cell type abundance

For estimating variation in cell type abundance at a variety of distance scales, we computed the coefficient of variation (CoV) in cell type abundance across a grid of regions in each tumor biopsy. First, we divided each tumor region into bins of size ranging from 0.3 x 0.3 mm to 10 x 10 mm. Let $Bins_I^k$ indicate the set of *I* bins for a given width *k* for a tumor sample. We then selected the subset $Bins_I^{k'}$ in which every bin $bin_i^{k'} \in Bins_I^{k'}$ that has at least 100 annotated cells. We computed the fractional abundance of each cell type in $bin_i^{k'}$ as $frac_{i,c}^{k'}$ where $c \in C$ is the set of all annotated cell types. Finally, we computed CoV_c^k to be coefficient of variation for a given cell type *c* at length scale *k*.

$$\Sigma_c^k = \sum_i frac_{i,c}^{k'} \ for \ i \ \in I \tag{68}$$

$$\mu_c^k = \frac{\Sigma_c^k}{card(I)} \tag{69}$$

$$\sigma_c^k = \sqrt{\frac{\sum_i (frac_{i,c}^{k'} - \mu_c^k)^2}{card(I)}} \tag{70}$$

$$CoV_c^k = \frac{\sigma_c^k}{\mu_c^k} \tag{71}$$

Experimental method details

10X Visium CytAssist spatial transcriptomics (ST-seq)

Tissue quality was determined by isolation of RNA from FFPE using the Qiagen RNeasy FFPE kit. Samples were then analyzed for tissue extraction quality using the Agilent 2100 bio-analyzer and Agilent RNA-6000 pico kit. For each sample, a DV200 score – the fraction of RNA fragments > 200 nucleotides in length – was calculated. Tissue quality for all samples was tested on unstained sections adjacent to the section used for ST-seq.

DLBCL samples were previously H&E stained. Imaging and coverslip removal were completed as described by 10X Protocol CG000518-Rev A and decrosslinking was performed according to 10X Protocol CG000520-Rev A[76,77]. NSCLC samples underwent deparaffinization, H&E staining, imaging, and decrosslinking according to CG000520-Rev B[78]. Sample imaging for all samples was performed using the Akoya Biosciences Vectra Polaris at 20X magnification.

We next performed the following steps as per either 10X Protocol CG000495-Rev A for the DLBCL samples or 10X Protocol CG000495-Rev E for the NSCLC samples[79,80]. First, samples underwent probe hybridization with Visium Human Transcriptome Probe Set v2.0, followed by probe ligation, and associated washes (**Supplementary Table 10**). Two native tissue slides and one Visium CytAssist 11 x 11 mm slide were then placed within the Visium CytAssist to enable RNA digestion, tissue removal, and transfer of ligated products onto the two fiducial frames of the Visium Slide. Next, we performed probe extension and elution off the Visium Slide, followed by pre-amplification and SPRIselect cleanup. For SPRIselect cleanup, DLBCL samples placed in only the 'High' position of the 10X magnetic separator, while NSCLC samples were placed in

1355 both 'High' and 'Low' positions according to CG000495-Rev E. To identify the optimal number of
1356 cycles for library amplification, we performed qPCR using Applied Biosciences QuantStudio 6
1357 Pro as per CG000495-Rev E (**Supplementary Table 4**). For this step, we included 0.5 μl of
1358 carboxy-X-rhodamine (ROX) with the DLBCL samples and not with the NSCLC samples.
1359 Sample Index PCR was run using the sample-specific optimal number of cycles, followed by:
1360 cleanup, Agilent TapeStation QC, sequencing, and demultiplexing using Bcl2fastq. Sample
1361 sequencing was performed on a NovaSeq 6000 for DLBCL samples and a NovaSeqX for
1362 NSCLC samples. Sample-specific parameters and QC are listed in **Supplementary Table 4**.
1363 For DLBCL experiments, we used the Applied Biosystems Veriti 96 well thermocycler, while for
1364 NSCLC samples we used the Eppendorf Mastercycler X50a and X50I.
1365
1366 **CODEX multiplexed immunofluorescence**
1367
1368 *Slide preparation*
1369 DLBCL samples were previously obtained as unstained slides mounted with 5 μm thickness
1370 formaldehyde-fixed, paraffin-embedded (FFPE) sections from the same patient biopsies as
1371 described in *'Patient samples'*. Coverslips were coated with 0.1% poly-l-lysine solution prior to
1372 mounting tissue sections to enhance adherence. The prepared coverslips were washed and
1373 stored according to guidelines from the CODEX user manual.
1374
1375 *Antibody preparation*
1376 Custom conjugated antibodies were conjugated using the CODEX conjugation kit as per the
1377 CODEX user manual (**Supplementary Table 8**). Briefly, the antibody is (1) partially reduced to
1378 expose thiol ends of the antibody heavy chains, (2) conjugated with a CODEX barcode, (3)
1379 purified, and (4) added to Antibody Storage Solution for long-term stabilization. Subsequently,
1380 antibody conjugation is verified using sodium dodecyl sulfate-polyacrylamide gel electrophoresis
1381 and with QC staining.
1382
1383 *Staining and data acquisition*
1384 Sample slides are stained following protocols in the CODEX User Manual. Briefly, samples are
1385 pretreated by heating at 60°C overnight, followed by deparaffinization, rehydration using ethanol
1386 washes, and antigen retrieval via immersion in Tris-EDTA pH 9.0 for 20 minutes. Samples are
1387 then blocked in staining buffer and incubated with the antibody cocktail for 3 hours at room
1388 temperature. After incubation, samples are washed and fixed following the CODEX User
1389 Manual. Data acquisition was performed using the PhenoCycler-Fusion 2.0 with a 20X
1390 objective, resulting in a resolution of 0.5 μm/pixel.
1391
1392 **Patient tumor PD-L1 IHC**
1393 FFPE biopsy samples were probed for PD-L1 expression using a qualitative
1394 immunohistochemical assay with the Dako 22C3 antibody (Pharm Dx kit). PD-L1 expression
1395 was classified using the Tumor Proportion Score (TPS), which represents the percentage of
1396 viable tumor cells that show partial or complete membrane staining. Normal background
1397 histiocytes served as internal controls to ensure quality of the PD-L1 staining. Quantification
1398 was performed by a board-certified pathologist as part of routine clinical care.
1399
1400 **Patient somatic mutation testing**
1401 The molecular profiles of the tumor biopsies were analyzed using Oncoplus or Oncoscreen, two
1402 Next Generation Sequencing (NGS) assays[81]. A description of patient mutation status can be
1403 found in **Supplementary Table 11**. Since the list of targeted genomic regions varied by the year
1404 in which testing was performed, a list of Oncoplus/Oncoscreen versions used for each patient

1405   as well as a list of the targeted genomic regions for each version can be found in
1406   **Supplementary Tables 11 and 12**, respectively.
1407
1408   For the Oncoplus analysis, DNA was isolated from the samples using the QIAamp DNA Blood
1409   Mini Kit (Qiagen), fragmented, and prepared into a sequencing library with patient-specific
1410   indexes (HTP Library Preparation Kit, Kapa Biosystems). Targeted genomic regions were
1411   enriched using a panel of biotinylated oligonucleotides (SeqCap EZ, Roche Nimblegen)
1412   supplemented with additional oligonucleotides (xGen Lockdown Probes, IDT). The enriched
1413   libraries were then sequenced on an Illumina HiSeq 2500 system, and the data was analyzed
1414   via bioinformatics pipelines against the hg19 (GRCh37) human genome reference sequence.
1415
1416   For Oncoscreen, DNA was isolated from formalin-fixed paraffin-embedded (FFPE) tumor tissue
1417   using the QIAamp DNA FFPE Tissue Kit (Qiagen). DNA was quantified using the Qubit
1418   fluorometric assay (Thermo Fisher Scientific) and a quantitative PCR assay (hgDNA
1419   Quantitation and QC kit, KAPA Biosystems). Targeted genomic regions were amplified using
1420   multiplex PCR (Thermo Fisher Scientific); PCR products were used to prepare NGS libraries
1421   with patient-specific adapter index sequences (HTP Library Preparation Kit, KAPA Biosystems).
1422   The enriched libraries were then sequenced on an Illumina MiSeq system, and the data was
1423   analyzed via bioinformatics pipelines against the hg19 (GRCh37) human genome reference
1424   sequence.
1425
1426   **Patient tumor volume measurements**
1427   For measurement of tumor volume changes over time, computed tomography (CT) imaging
1428   reports were obtained for patients in the NSCLC as permitted by the IRBs referenced in 'Patient
1429   samples'. For patients with measurable disease at the time of treatment start (denoted as month
1430   zero), the largest lesion was identified and labeled the 'index lesion'. Changes in index lesions
1431   were collected when described in serial reports by a board-certified radiologist as part of routine
1432   clinical care.
1433
1434   **<u>Subject details</u>**
1435
1436   **Patient samples**
1437   Non-small cell lung cancer (NSCLC) patients were treated with immune checkpoint blockade
1438   therapy +/- chemotherapy at the University of Chicago Medical Center (Chicago, IL). All patients
1439   provided written informed consent for the collection and study of pre-treatment diagnostic tumor
1440   biopsy samples and for clinical outcomes including treatment regimen, treatment-related
1441   toxicities, and disease outcomes, as approved by the University of Chicago Institutional Review
1442   Board (IRB 9571 and IRB 24-0063). For the ST-seq analysis, 16 tumor samples were collected
1443   prior to therapy initiation, each from a separate patient. Inclusion criteria for these patients
1444   included (1) NSCLC stage IV patients either at initial presentation or as progression from
1445   previously treated early-stage disease, (2) biopsy of either the primary tumor or a metastatic
1446   tumor performed and stored within 6 months prior to treatment in the metastatic setting, (3)
1447   subsequent first line treatment with anti-PD1/anti-PD-L1 immune checkpoint blockade (ICB) with
1448   or without platinum-based chemotherapy. Exclusion criteria included (1) no prior therapy in the
1449   metastatic setting and (2) less than 2 doses of ICB therapy administered. We selected the first
1450   16 patients that met these criteria and that had an available FFPE tumor biopsy block. From the
1451   archival block, a fresh 5 μm section was cut and placed on a standard slide for use in ST-seq
1452   protocols (see '*10X Visium spatial transcriptomics (ST-seq)*'). Progression was defined as time
1453   from the first dose of ICB until either radiographic or symptom-based evidence of disease
1454   progression. ICB regimen, ICB treatment duration, reason for ICB discontinuation, time to

1455   progression following ICB start, and time to death following ICB start are listed for all patients
1456   (**Supplementary Table 11**).

1457

1458   Diffuse large B-cell lymphoma (DLBCL) patients were treated at the University of Chicago
1459   Medical Center (Chicago, IL). All patients provided written informed consent for the collection
1460   and study of pre-treatment diagnostic tumor biopsy samples and for clinical outcomes including
1461   treatment regimen, treatment-related toxicities, and disease outcomes, as approved by the
1462   University of Chicago Institutional Review Board (IRB 13-1297). Each biopsy was reviewed by 2
1463   hematopathologists for diagnostic confirmation. Biopsy slides were previously cut from FFPE
1464   sections and H&E stained for prior studies[82].

1465

1466   **Supplementary Tables**

1467

1468   **Supplementary Table 1.** Pan-tumor database properties

1469

1470   **Supplementary Table 2.** Differential gene and pathway spatial lability amongst pan-tumor
1471   SLAB classes

1472

1473   **Supplementary Table 3.** Bulk gene sets for prediction of NSCLC ICB response

1474

1475   **Supplementary Table 4.** ST-seq QC Metrics

1476

1477   **Supplementary Table 5.** Reactome pathway list

1478

1479   **Supplementary Table 6.** KEGG pathway list

1480

1481   **Supplementary Table 7.** SpaCET input cancer types

1482

1483   **Supplementary Table 8.** CODEX Antibody Targets

1484

1485   **Supplementary Table 9.** ST versus IF Cell Type Classification

1486

1487   **Supplementary Table 10.** Visium Human Transcriptome Probe Set v2.0 - Probe Set
1488   Reference CSV file

1489

1490   **Supplementary Table 11.** NSCLC Clinical Metadata (oncoplus version)

1491

1492   **Supplementary Table 12.** Oncoplus/Oncoscreen Gene Panels

1493

References

1.   Arneth, B. Tumor microenvironment. *Med.* **56**, (2020).

2.   Anderson, N. M. & Simon, M. C. The tumor microenvironment. *Curr. Biol.* **30**, R921–R925 (2020).

3.   Bressan, D., Battistoni, G. & Hannon, G. J. The dawn of spatial omics. *Science (New York, N.Y.)* vol. 381 eabq4964 (2023).

4.   Burgos-Panadero, R. *et al.* The tumour microenvironment as an integrated framework to understand cancer biology. *Cancer Lett.* **461**, 112–122 (2019).

5.   Giraldo, N. A. *et al.* The clinical role of the TME in solid cancer. *Br. J. Cancer* **120**, 45–53 (2019).

6.   Azimi, F. *et al.* Tumor-infiltrating lymphocyte grade is an independent predictor of sentinel lymph node status and survival in patients with cutaneous melanoma. *J. Clin. Oncol.* **30**, 2678–2683 (2012).

7.   Thomas, N. E. *et al.* Tumor-infiltrating lymphocyte grade in primary melanomas is independently associated with melanoma-specific survival in the population-based genes, environment and melanoma study. *J. Clin. Oncol.* **31**, 4252–4259 (2013).

8.   Pagès, F. *et al.* International validation of the consensus Immunoscore for the classification of colon cancer: a prognostic and accuracy study. *Lancet* **391**, 2128–2139 (2018).

9.   Marliot, F. *et al.* Analytical validation of the Immunoscore and its associated prognostic value in patients with colon cancer. *J. Immunother. Cancer* **8**, 13–15 (2020).

10.   Bruni, D., Angell, H. K. & Galon, J. The immune contexture and Immunoscore in cancer prognosis and therapeutic efficacy. *Nat. Rev. Cancer* **20**, 662–680 (2020).

11.   Park, Y. M. & Lin, D. C. Moving closer towards a comprehensive view of tumor biology and microarchitecture using spatial transcriptomics. *Nat. Commun.* **14**, 14–16 (2023).

12.   Ali, H. R. *et al.* Imaging mass cytometry and multiplatform genomics define the

1520   phenogenomic landscape of breast cancer. *Nat. cancer* **1**, 163–175 (2020).

1521   13.   Danenberg, E. *et al.* Breast tumor microenvironment structures are associated with

1522   genomic features and clinical outcome. *Nat. Genet.* **54**, 660–669 (2022).

1523   14.   Schürch, C. M. *et al.* Coordinated Cellular Neighborhoods Orchestrate Antitumoral

1524   Immunity at the Colorectal Cancer Invasive Front. *Cell* **182**, 1341-1359.e19 (2020).

1525   15.   Gaglia, G. *et al.* Temporal and spatial topography of cell proliferation in cancer. *Nat. Cell*

1526   *Biol.* **24**, 316–326 (2022).

1527   16.   Nirmal, A. J. *et al.* The Spatial Landscape of Progression and Immunoediting in Primary

1528   Melanoma at Single-Cell Resolution. *Cancer Discov.* **12**, 1518–1541 (2022).

1529   17.   Greenwald, A. C. *et al.* Integrative spatial analysis reveals a multi-layered organization of

1530   glioblastoma. *Cell* **187**, 2485-2501.e26 (2024).

1531   18.   Du, J. *et al.* Advances in spatial transcriptomics and related data analysis strategies. *J.*

1532   *Transl. Med.* **21**, 1–21 (2023).

1533   19.   Halabi, N., Rivoire, O., Leibler, S. & Ranganathan, R. Protein Sectors: Evolutionary Units

1534   of Three-Dimensional Structure. *Cell* **138**, 774–786 (2009).

1535   20.   Russ, W. P., Lowery, D. M., Mishra, P., Yaffe, M. B. & Ranganathan, R. Natural-like

1536   function in artificial WW domains. *Nature* **437**, 579–583 (2005).

1537   21.   Russ, W. P. *et al.* An evolution-based model for designing chorismate mutase enzymes.

1538   *Science (80-.).* **369**, 440–445 (2020).

1539   22.   McLaughlin, R. N., Poelwijk, F. J., Raman, A., Gosal, W. S. & Ranganathan, R. The

1540   spatial architecture of protein function and adaptation. *Nature* **491**, 138–142 (2012).

1541   23.   Eisen, J. A. Phylogenomics: Improving functional predictions for uncharacterized genes

1542   by evolutionary analysis. *Genome Res.* **8**, 163–167 (1998).

1543   24.   Pellegrini, M., Marcotte, E. M., Thompson, M. J., Eisenberg, D. & Yeates, T. O. Assigning

1544   protein functions by comparative genome analysis: Protein phylogenetic profiles. *Proc.*

1545   *Natl. Acad. Sci. U. S. A.* **96**, 4285–4288 (1999).

25. Cong, Q., Anishchenko, I., Ovchinnikov, S. & Baker, D. Protein interaction networks revealed by proteome coevolution. *Science (80-.).* **365**, 185–189 (2019).

26. Zaydman, M. A. *et al.* Defining hierarchical protein interaction networks from spectral analysis of bacterial proteomes. *Elife* **11**, (2022).

27. Jia, J. *et al.* Conserved Covarying Gut Microbial Network in Preterm Infants and Childhood Growth During the First 5 Years of Life: A Prospective Cohort Study. *Am. J. Clin. Nutr.* **118**, 561–571 (2023).

28. Raman, A. S. *et al.* A sparse covarying unit that describes healthy and impaired human gut microbiota development. *Science (80-.).* **365**, (2019).

29. Geesink, P., Horst, J. ter & Ettema, T. J. G. More than the sum of its parts: uncovering emerging effects of microbial interactions in complex communities. *FEMS Microbiol. Ecol.* **100**, 1–7 (2024).

30. 10x Genomics. Visium Spatial Gene Expression for FFPE Reagent Kits Reagent Kits, Document Number CG000047 Rev E. 1–47 (2024).

31. Walker, B. L. NeST : nested hierarchical structure identification in spatial transcriptomic data. *Nat. Commun.* 1–17 (2023) doi:10.1038/s41467-023-42343-x.

32. Lin, X., Gao, L., Whitener, N., Ahmed, A. & Wei, Z. A model-based constrained deep learning clustering approach for spatially resolved single-cell data. *Genome Res.* **32**, 1906–1917 (2022).

33. Dong, K. & Zhang, S. Deciphering spatial domains from spatially resolved transcriptomics with an adaptive graph attention auto-encoder. *Nat. Commun.* **13**, 1–12 (2022).

34. Long, Y. *et al.* Spatially informed clustering, integration, and deconvolution of spatial transcriptomics with GraphST. *Nat. Commun.* **14**, 1–19 (2023).

35. Hu, J. *et al.* SpaGCN: Integrating gene expression, spatial location and histology to identify spatial domains and spatially variable genes by graph convolutional network. *Nat. Methods* **18**, 1342–1351 (2021).

36. Tian, T., Zhang, J., Lin, X., Wei, Z. & Hakonarson, H. Dependency-aware deep generative models for multitasking analysis of spatial omics data. *Nat. Methods* (2024) doi:10.1038/s41592-024-02257-y.

37. Haviv, D., Gatie, M., Hadjantonakis, A.-K., Nawy, T. & Pe'er, D. The covariance environment defines cellular niches for spatial inference. *Nat. Biotechnol.* (2024) doi:10.1038/s41587-024-02193-4.

38. Doran, B. A. *et al.* An evolution-based framework for describing human gut bacteria. *bioRxiv* 2023.12.04.569969 (2023) doi:10.1101/2023.12.04.569969.

39. Ru, B., Huang, J., Zhang, Y., Aldape, K. & Jiang, P. Estimation of cell lineages in tumors from spatial transcriptomics data. *Nat. Commun.* **14**, (2023).

40. Zhu, H., Yu, X., Zhang, S. & Shu, K. Targeting the Complement Pathway in Malignant Glioma Microenvironments. *Front. Cell Dev. Biol.* **9**, 1–16 (2021).

41. Gruenbacher, G. *et al.* The human G protein-coupled ATP receptor P2Y11 is associated with IL-10 driven macrophage differentiation. *Front. Immunol.* **10**, 1–13 (2019).

42. Batlle, E. & Massagué, J. Transforming Growth Factor-β Signaling in Immunity and Cancer. *Immunity* **50**, 924–940 (2019).

43. Sharif, H. *et al.* Dipeptidyl peptidase 9 sets a threshold for CARD8 inflammasome formation by sequestering its active C-terminal fragment. *Immunity* **54**, 1392-1404.e10 (2021).

44. Geiss-Friedlander, R. *et al.* The cytoplasmic peptidase DPP9 is rate-limiting for degradation of proline-containing peptides. *J. Biol. Chem.* **284**, 27211–27219 (2009).

45. Huang, N. *et al.* TRIM family contribute to tumorigenesis, cancer development, and drug resistance. *Exp. Hematol. Oncol.* **11**, 1–22 (2022).

46. Xu, X. & Jin, T. ELMO proteins transduce G protein-coupled receptor signal to control reorganization of actin cytoskeleton in chemotaxis of eukaryotic cells. *Small GTPases* **10**, 271–279 (2019).

1598   47.   Ding, Z. C. *et al.* Persistent STAT5 activation reprograms the epigenetic landscape in

1599   CD4+ T cells to drive polyfunctionality and antitumor immunity. *Sci. Immunol.* **5**, 1–18

1600   (2020).

1601   48.   Zhu, L. *et al.* Dapl1 controls NFATc2 activation to regulate CD8+ T cell exhaustion and

1602   responses in chronic infection and cancer. *Nat. Cell Biol.* **24**, 1165–1176 (2022).

1603   49.   Richard, A. C., Frazer, G. L., Ma, C. Y. & Griffiths, G. M. Staggered starts in the race to T

1604   cell activation. *Trends Immunol.* **42**, 994–1008 (2021).

1605   50.   Voros, O., Panyi, G. & Hajdu, P. Immune synapse residency of orai1 alters ca2+

1606   response of t cells. *Int. J. Mol. Sci.* **22**, (2021).

1607   51.   Yim, K. H. W., Hrout, A. Al, Borgoni, S. & Chahwan, R. Extracellular vesicles orchestrate

1608   immune and tumor interaction networks. *Cancers (Basel).* **12**, 1–23 (2020).

1609   52.   Chen, R. & Chen, L. Solute carrier transporters: emerging central players in tumour

1610   immunotherapy. *Trends Cell Biol.* **32**, 186–201 (2022).

1611   53.   Pan, Y. *et al.* RNA Dysregulation: An Expanding Source of Cancer Immunotherapy

1612   Targets. *Trends Pharmacol. Sci.* **42**, 268–282 (2021).

1613   54.   Srivastava, A. K., Guadagnin, G., Cappello, P. & Novelli, F. Post-Translational

1614   Modifications in Tumor-Associated Antigens as a Platform for Novel Immuno-Oncology

1615   Therapies. *Cancers (Basel).* **15**, (2023).

1616   55.   Martin, A. L. *et al.* Olfactory Receptor OR2H1 Is an Effective Target for CAR T Cells in

1617   Human Epithelial Tumors. *Mol. Cancer Ther.* **21**, 1184–1194 (2022).

1618   56.   Garassino, M. C. *et al.* Pembrolizumab Plus Pemetrexed and Platinum in Nonsquamous

1619   Non-Small-Cell Lung Cancer: 5-Year Outcomes from the Phase 3 KEYNOTE-189 Study.

1620   *J. Clin. Oncol.* **41**, 1992–1998 (2023).

1621   57.   Hallqvist, A., Rohlin, A. & Raghavan, S. Immune checkpoint blockade and biomarkers of

1622   clinical response in non–small cell lung cancer. *Scand. J. Immunol.* **92**, 1–10 (2020).

1623   58.   Mino-Kenudson, M. *et al.* Predictive Biomarkers for Immunotherapy in Lung Cancer:

1624   Perspective From the International Association for the Study of Lung Cancer Pathology

1625   Committee. *J. Thorac. Oncol.* **17**, 1335–1354 (2022).

1626   59.   Li, X. *et al.* The Notch signaling pathway: a potential target for cancer immunotherapy. *J.*

1627   *Hematol. Oncol.* **16**, 1–31 (2023).

1628   60.   Hegde, P. S. & Chen, D. S. Top 10 Challenges in Cancer Immunotherapy. *Immunity* **52**,

1629   17–35 (2020).

1630   61.   Clifton, G. T. *et al.* Developing a definition of immune exclusion in cancer: results of a

1631   modified Delphi workshop. *J. Immunother. Cancer* **11**, e006773 (2023).

1632   62.   Klema, V. & Laub, A. The singular value decomposition: Its computation and some

1633   applications. *IEEE Trans. Automat. Contr.* **25**, 164–176 (1980).

1634   63.   Ehman, E. C. *et al.* Renewing Felsenstein's phylogenetic bootstrap in the era of Big Data.

1635   *Nature* **556**, 452–456 (2018).

1636   64.   Ripley, B. D. The Second-Order Analysis of Stationary Point Processes. *J. Appl. Probab.*

1637   **13**, 255–266 (1976).

1638   65.   Ripley, B. D. *Statistical Inference for Spatial Processes*. (Cambridge University Press,

1639   1988). doi:DOI: 10.1017/CBO9780511624131.

1640   66.   Morris, J. A. & Gardner, M. J. Calculating confidence intervals for relative risks (odds

1641   ratios) and standardised ratios and rates. *Br. Med. J. (Clin. Res. Ed).* **296**, 1313–1316

1642   (1988).

1643   67.   Benjamini, Y. & Hochberg, Y. Controlling the False Discovery Rate: A Practical and

1644   Powerful Approach to Multiple Testing. *J. R. Stat. Soc. Ser. B* **57**, 289–300 (1995).

1645   68.   Sokal, R. R. & C.D.Michener. A Statistical Method for Evaluating Systematic

1646   Relationships. *Univ. Kansas Sci. Bull.* **28**, 1409–1438 (1958).

1647   69.   Subramanian, A. *et al.* Gene set enrichment analysis: A knowledge-based approach for

1648   interpreting genome-wide expression profiles. *Proc. Natl. Acad. Sci. U. S. A.* **102**, 15545–

1649   15550 (2005).

1650 70. Fabregat, A. *et al.* The Reactome pathway Knowledgebase. *Nucleic Acids Res.* **44**,

1651 D481–D487 (2016).

1652 71. Chen, E. Y. *et al.* Enrichr: interactive and collaborative HTML5 gene list enrichment

1653 analysis tool. *BMC Bioinformatics* **14**, 128 (2013).

1654 72. Hänzelmann, S., Castelo, R. & Guinney, J. GSVA: Gene set variation analysis for

1655 microarray and RNA-Seq data. *BMC Bioinformatics* **14**, (2013).

1656 73. Kanehisa, M. & Goto, S. KEGG: Kyoto Encyclopedia of Genes and Genomes. *Nucleic*

1657 *Acids Res.* **28**, 27–30 (2000).

1658 74. Greenwald, N. F. *et al.* Whole-cell segmentation of tissue images with human-level

1659 performance using large-scale data annotation and deep learning. *Nat. Biotechnol.* **40**,

1660 555–565 (2022).

1661 75. van der Walt, S. *et al.* scikit-image: image processing in Python. *PeerJ* **2**, e453 (2014).

1662 76. 10X Genomics. Visium Spatial Gene Expression for FFPE - Tissue Preparation Guide.

1663 *Doc. Number CG000518 Rev A* (2022).

1664 77. 10X Genomics. Visium Spatial Gene Expression for FFPE – Deparaffinization, H&E

1665 Staining, Imaging & Decrosslinking. *Doc. Number CG000520 Rev A* (2022).

1666 78. 10X Genomics. Visium Spatial Gene Expression for FFPE – Deparaffinization, H&E

1667 Staining, Imaging & Decrosslinking. *Doc. Number CG000520 Rev B* (2022).

1668 79. 10X Genomics. Visium CytAssist Spatial Gene Expression Reagent Kits. *Doc. Number*

1669 *CG000495 Rev A* (2022).

1670 80. 10X Genomics. Visium CytAssist Spatial Gene Expression Reagent Kits. *Doc. Number*

1671 *CG000495 Rev E* (2023).

1672 81. Kadri, S. *et al.* Clinical Validation of a Next-Generation Sequencing Genomic Oncology

1673 Panel via Cross-Platform Benchmarking against Established Amplicon Sequencing

1674 Assays. *J. Mol. Diagnostics* **19**, 43–56 (2017).

1675 82. Godfrey, J. *et al.* PD-L1 gene alterations identify a subset of diffuse large B-cell

1676   lymphoma harboring a T-cell–inflamed phenotype. *Blood* **133**, 2279–2290 (2019).

1677

Acknowledgements

We thank D. Pincus, M. Mani, M. Lingen, D. Zemmour, I. Moskowitz, and R. Ranganathan for helpful discussions. We thank the genomics core and human immunologic monitoring core facilities at the University of Chicago for their aid in sequencing and imaging our ST-seq samples. This work was supported by the Duchossois Family Institute, the Department of Pathology, and the Center for the Physics of Evolving Systems at the University of Chicago. Funding for V.B. was provided by a T32 NIH training grant within the Department of Medicine, Section of Hematology/Oncology at the University of Chicago.

Author contributions

H.G. performed all ST-seq data collection including preparing samples and running the 10X Visium platform. U.P. provided critical conceptual guidance in writing the manuscript and conducted portions of analysis related to Figs. 3, 4, and Extended Data Fig. 10. A.D.L., A.E., A.P., C.M.B. aided in data collection of the NSCLC samples. A.D.L. aided in the writing of the Methods section. C.M.B. provided critical feedback for our manuscript. B.A.D. provided critical conceptual guidance as well as technical support in writing of the code used for TumorSPACE. J.K. provided diffuse large B cell lymphoma samples for ST-seq and conceptual guidance. M.C.G. leads the lung cancer biobank at the University of Chicago, established the IRB required for collecting ST-seq data on the NSCLC samples, and provided critical feedback for our manuscript. V.B. performed all analysis, wrote all code, and coordinated all data collection efforts. V.B. and A.S.R. conceived of the project and A.S.R. provided supervision for all aspects of analysis and data collection. V.B. and A.S.R. wrote the paper.

Competing interests

All authors declare no competing interests.

1704 **Data and materials availability**

1705 All data relevant to our manuscript can be found within associated Supplementary Tables. All

1706 ST-seq data related to the cohort of DLBCL and NSCLC patients will be available for download

1707 in the Gene Expression Omnibus (GEO) database upon assignment of an accession number.

1708

1709 **Code availability**

1710 All code, along with annotations and step-wise instructions, will be available for download via

1711 github repository upon publication of our manuscript:

1712 https://github.com/aramanlab/TumorSPACE.jl

1713

1714 **Ethics Declaration**

1715 Patents (63/572,XXX) related to this research have been filed by the University of Chicago with

1716 V.B. and A.S.R. as inventors.

1717

1718 **Materials and Correspondence**

1719 Author to whom correspondence and materials requested should be addressed is A.S.R.